

1 **Alaskan-type Kedanshan intrusive complex, central Inner**  
2 **Mongolia, China: Superimposed subduction between the**  
3 **Mongol-Okhotsk and Paleo-Pacific oceans in the Jurassic**

4

5 Jinlong Dong <sup>a</sup>, Shuguang Song <sup>a\*</sup>, Mingming Wang <sup>a</sup>, Mark B. Allen <sup>b</sup>, Li Su<sup>c</sup>,  
6 Chao Wang <sup>a</sup>, Liming Yang <sup>a</sup>, Bei Xu <sup>a</sup>

7 <sup>a</sup> *MOE Key Laboratory of Orogenic Belts and Crustal Evolution, School of Earth and Space Science,*  
8 *Peking University, Beijing, China*

9 <sup>b</sup> *Department of Earth Sciences, University of Durham, Durham, UK*

10 <sup>c</sup> *Institute of Geology and Geophysics, Chinese Academy of Science, Beijing, China*

11

12 \* Corresponding author: [Shuguang Song](mailto:sgsong@pku.edu.cn)

13 [Email: sgsong@pku.edu.cn](mailto:sgsong@pku.edu.cn)

14 MS for *Journal of Asian Earth Sciences* (special issue for Prof. Jahn Part 2)

15

## 16 **Abstract**

17       The Xing'an-Inner Mongolia accretionary belt in the eastern Central Asian Orogenic  
18 Belt (CAOB) was produced by the subduction of three oceanic plates: the Paleo-Asian,  
19 Mongol-Okhotsk and Paleo-Pacific oceans. The interactions between these plates remain  
20 unclear. Here we report an Alaskan-type ultramafic-mafic intrusive complex in the  
21 Kedanshan area, central Inner Mongolia, China. The main lithologies of this intrusive  
22 complex include cumulate dunite, pyroxene peridotite, olivine pyroxenite and cumulate  
23 gabbro, with late gabbroic/anorthositic veins. Minerals and whole-rock compositional  
24 variations display characteristics of an arc cumulate trend (Alaskan-type), through  
25 fractional crystallization of Mg-rich and hydrous basaltic magma associated with oceanic  
26 subduction. Zircons from gabbro samples yield long-lived Jurassic ages of  $\sim 193 \pm 6$  Ma to  
27  $179 \pm 4$  Ma. We conclude that this ultramafic-mafic complex is an accumulated intrusion  
28 from an arc-related, high-Mg magma chamber in the metasomatized mantle wedge above  
29 a subduction zone. Considering the ages, location and tectonic setting of the complex, we  
30 suggest that it was most likely generated by melting of a large and triangle-shaped mantle  
31 wedge during superimposed subduction between the Mongol-Okhotsk Ocean and the  
32 Paleo-Pacific Ocean in the Jurassic.

33 *Keywords:* Alaskan-type ultramafic-mafic intrusion; Jurassic; Superimposed subduction;  
34 Mongol-Okhotsk Ocean; Paleo-Pacific Ocean

## 35 **1. Introduction**

36       Ultramafic-mafic rock complexes provide keys to understanding the mantle

37 compositions, deep geodynamic processes and the tectonic setting of their host intrusions  
38 (e.g., [KePezhinskas et al., 1997](#); [Meibom et al., 2002](#); [Polat et al., 2011](#)). Many  
39 ultramafic-mafic rocks, including mantle peridotites and cumulates in the lower part of  
40 ophiolites, are commonly associated with mineral resources such as Fe, V, Ni, Cu and the  
41 platinum group elements (PGE). Alaskan-type complexes are characterized by a concentric  
42 layout of rock types, e.g., a cumulate dunite core surrounded by wehrlite, olivine  
43 clinopyroxenite, clinopyroxenite, magnetite -hornblende clinopyroxenite, hornblendite and  
44 gabbro. Such complexes are considered to be the mark of island arc or  
45 active continental margin settings ([Murray, 1972](#); [Tistl et al, 1994](#); [Helmy and EI](#)  
46 [Mahallawi, 2003](#); [Thakurta et al., 2008](#); [Zhang., 2014](#)) and closely related to PGE  
47 mineralization ([Irvine, 1974](#); [Ishiwatari and Ichiyama, 2004](#); [Thakurta et al., 2008](#); [Ripley,](#)  
48 [2009](#); [Su et al., 2013](#)). Therefore, understanding of the petrogenesis, tectonic environment  
49 and source characteristics of ultramafic-mafic rocks is significant for reconstructing the  
50 regional geological evolution.

51 Central Inner Mongolia is located in the southeastern segment of the Central Asian  
52 Orogenic Belt (CAOB). In this region, three tectonic domains join together, including the  
53 Paleo-Asian Ocean tectonic domain itself, and the Mongol-Okhotsk Ocean in the north  
54 and Paleo-Pacific Ocean tectonic domain in the east (e.g., [Zonenshain et al., 1990](#); [Zorin,](#)  
55 [1999](#); [Sorokin et al., 2004](#); [Wu et al., 2011](#); [Xu et al., 2013a](#); [Xu et al., 2013b, 2015](#);  
56 [Wang et al., 2011, 2012, 2015a](#)). The CAOB was produced by the long-lived subduction  
57 and eventual closure of the Paleo-Asian Ocean and by the convergence between the

58 North China Craton and the Mongolian micro-continent (e.g., [Xiao et al., 2003, 2009;](#)  
59 [Song et al., 2015](#)). The Mongol-Okhotsk Ocean was a large embayment of the  
60 Paleo-Pacific Ocean ([Zonenshain et al., 1990; Zorin et al., 1999; Donskaya et al., 2013](#)),  
61 and it played a significant role in the tectonic evolution of the eastern part of Eurasia  
62 since the Mesozoic (e.g., [Xu et al., 2013a; Tang et al., 2014](#)). The Paleo-Pacific Oceanic  
63 domain was produced by the westward subduction of the Izanagi Plate, which controlled  
64 the evolution of the East Asian continental margin since the Mesozoic (e.g., [Guo et al.,](#)  
65 [2007; Wu et al., 2011](#)). Ultramafic-mafic blocks crop out in central Inner Mongolia, and  
66 most of them have been shown to be the basal part of the Paleozoic ophiolitic sequences.  
67 Based on ages of the ophiolite suites, most researchers suggested that the closure time of  
68 the Paleo-Asian Ocean was in the Late Permian or Early Triassic (e.g., [Xiao et al., 2003,](#)  
69 [2009; Li et al., 2012a; Jian et al., 2012; Cheng et al., 2014; Song et al., 2015; Guo et al.,](#)  
70 [2016](#)). However, Late Mesozoic ultramafic-mafic outcrops in central Inner Mongolia are  
71 sparsely documented. In general, Early Jurassic (204-180 Ma) magmatic records are  
72 scarce in this region ([Tong et al., 2010; Wang et al., 2015a](#)).

73 The Kedanshan ultramafic-mafic intrusion has long been regarded as a component  
74 of ophiolite associated with the Paleo-Asian Ocean. In this paper, we present a  
75 comprehensive study, including petrologic, mineralogical, geochemical and chronological  
76 data, for this intrusion. We confirm that it is an Alaskan-type complex that formed in the  
77 Jurassic (193-179 Ma). These data provide evidence for superimposed subduction  
78 between the Mongol-Okhotsk Ocean and the Paleo-Pacific Ocean in the Jurassic.

## 79 **2. Geological background**

80 The Kedanshan ultramafic-mafic intrusion is located ~80 km southwest of Linxi in  
81 central Inner Mongolia (Fig. 1). Tectonically, it is located within the Solonker-Linxi SSZ  
82 ophiolite belt of the Xing'an-Inner Mongolia accretionary belt (XIMAB) of the CAOB.  
83 To the north is the Mongol-Okhotsk orogenic belt (Fig.1A) and to the east is the western  
84 part of the Paleo-Pacific subduction zone (Fig.1A). The Mongol-Okhotsk orogenic belt is  
85 located between northern Mongolia and Siberia Craton and extends over 3000 km in a  
86 northeast-southwest orientation (Fig. 1A). The closure of the Mongol-Okhotsk Ocean  
87 was suggested to have occurred in a scissor-like style that started in the Triassic-Late  
88 Jurassic (Zonenshain et al., 1990) or Early Middle Jurassic (Zorin, 1999) from the west,  
89 and finished in the Late Jurassic-Early Cretaceous to the east (Cogné et al., 2005). The  
90 Paleo-Pacific tectonic domain is associated with westward subduction of the  
91 Paleo-Pacific Ocean in the Early Mesozoic (Wu et al., 2007; Zhou and Wilde, 2013; Zhou  
92 et al., 2014; Wang et al., 2015a; Niu et al., 2015). The XIMAB comprises a series of  
93 suture zones, arcs, micro-continental blocks and orogenic belts between the North China  
94 Craton and the Mongolia micro-continent, and occurred chiefly during the Paleozoic  
95 (Fig.1B, Xiao et al., 2003, 2009; Miao et al., 2007, 2008; Jian et al., 2012; Xu et al.,  
96 2013b, 2015; Zhao et al., 2014; Song et al., 2015).

97 The studied region consists of Ordovician (Baoerhantu Group) and Late Jurassic  
98 sedimentary-volcanic strata (Manketouebo Group), and intrusive rocks including the  
99 Kedanshan ultramafic-mafic complex and a Late Jurassic monzonite granite (Fig.1C).

100 The Ordovician strata (Baoerhantu Group) consist mainly of metamorphic sandstone  
101 and siliceous rock and occupy an area of less than 40 km<sup>2</sup>. The Late Jurassic  
102 sedimentary-volcanic strata consist of rhyolitic ignimbrite, rhyolitic volcanic breccia,  
103 rhyolite, reworked tuff and tuffaceous sandstone.

### 104 **3. Petrography**

105 The Kedanshan ultramafic-mafic intrusion is ~1.7 km long and ~1.2 km wide and  
106 occupies an area of ~1.4 km<sup>2</sup>. Except for off-white gabbro and anorthosite, most rocks in  
107 the Kedanshan ultramafic-mafic intrusion are dark colored, showing weak striped texture  
108 and strong serpentinization, which makes it difficult to distinguish lithologies in the field  
109 (Fig. 2). The off-white gabbro/anorthosite occurs either as veins (Fig. 2A and C) or as  
110 interlayers with peridotite (Fig. 2B). The layered gabbro shows an obvious cumulate  
111 structure in the field (Fig. 2D). According to the mineral assemblage and modal contents,  
112 five distinct lithologic types can be recognized (Fig. 3): (1) dunite, (2) pyroxene  
113 peridotite, (3) olivine pyroxenite, (4) pyroxenite and gabbro, and (5) gabbro/anorthosite  
114 veins.

#### 115 **3.1 Dunite**

116 Olivine grains in dunite are totally serpentinized. Some dunite samples contain  
117 nearly 100 vol.% olivine with ~2 vol.% chromian spinel, and others have small amount  
118 of clinopyroxene (<10 vol.%). They show medium- to coarse-grained inequigranular to  
119 granoblastic textures without deformation (Fig. 3A to C). The serpentinized olivine is  
120 oval-shaped, subhedral crystals with size ranging from 0.5 to 1.5 mm, and displays

121 typical cumulate texture with orientated long-axes. Clinopyroxene grains (0.1 to 0.5 mm)  
122 occur as intercumulus grains between olivines (Fig. 3B and C). Chromian spinel consists  
123 of disseminated euhedral to subhedral crystals between and within other minerals (Fig.  
124 3A to C).

### 125 **3.2 Peridotite**

126 The peridotite consists of olivine (~40-70 vol.%), clinopyroxene (~30-50 vol.%),  
127 orthopyroxene (~5-10 vol.%) and chrome spinel (~3-4 vol.%), showing a massive micro-  
128 to fine-grained granoblastic texture (Fig. 3D). Olivine grains in peridotite were partly  
129 serpentized (Fig. 3D) along cracks or grain boundaries (Fig. 3D). Clinopyroxene occurs  
130 as either dispersed grains or intercumulus between olivine crystals (Fig. 3D).  
131 Disseminated chromian spinels (~0.05 to 0.2 mm) occur as euhedral to subhedral grains,  
132 and they are partially or totally included in silicate minerals indicating their early  
133 crystallization.

### 134 **3.3 Olivine pyroxenite**

135 The olivine pyroxenite consists mainly of 70-80 vol.% clinopyroxene and 5-30 vol.%  
136 olivine with less than 10 vol.% orthopyroxene and opaque minerals (Fig. 3E and F). It  
137 shows medium-grained inequigranular or granoblastic textures (Fig. 3E and F).  
138 Clinopyroxene grains are subhedral to euhedral and vary in size (0.1 to 1.5 mm) (Fig. 3E  
139 and F). Olivine forms euhedral crystals (0.1 to 0.4 mm) and occurs intercumulus between  
140 pyroxene grains (Fig. 3E and F).

### 141 **3.4 Pyroxenite and gabbro**

142 Lithologies of the layered gabbro vary from Pl-poor pyroxenite to Pl-rich gabbro  
143 with the modal change of 15-70 vol.% plagioclase, 10-55 vol.% clinopyroxene, 2-8 vol.%  
144 orthopyroxene with minor sulfide (Fig. 3G to I). They have medium- to fine-grained  
145 textures, and display characteristic cumulate features with abundant clinopyroxene and  
146 plagioclase (Fig. 3G to I). Orthopyroxene occurs as subhedral, crystals in concordance  
147 with Cpx (Fig. 3G). Plagioclase crystals are strongly altered (Fig. 3G to I); they occur as  
148 either interstitial phases between pyroxene grains, or enclose clinopyroxene crystals,  
149 indicating their late crystallization (Fig. 3G to I).

## 150 **4. Analytical methods**

### 151 **4.1 Mineral chemistry**

152 Mineral analyses were done on a JEOL JXA-8100 Electron Probe Microanalyzer  
153 (EPMA) at Peking University. Analytical conditions were optimized for standard silicates  
154 and oxides at 15 kV accelerating voltage with a 20 nA focused beam current for all the  
155 elements. Routine analyses were obtained by counting for 30 seconds at peak and 10  
156 seconds on background. Repeated analysis of natural and synthetic mineral standards  
157 yielded precisions better than  $\pm 2\%$  for most elements.

### 158 **4.2 Whole-rock major and trace element analyses**

159 Based on careful petrographic observation, we selected thirteen samples for using  
160 whole rock major and trace element analyses. These representative samples include  
161 dunite, pyroxene peridotite, olivine pyroxenite, and gabbro. Whole-rock major element



162 oxides ( $\text{SiO}_2$ ,  $\text{TiO}_2$ ,  $\text{Al}_2\text{O}_3$ ,  $\text{FeO}$ ,  $\text{MnO}$ ,  $\text{MgO}$ ,  $\text{CaO}$ ,  $\text{Na}_2\text{O}$ ,  $\text{K}_2\text{O}$ , and  $\text{P}_2\text{O}_5$ ) were  
163 determined using inductively coupled plasma-optical emission spectroscopy (ICP-OES)  
164 at China University of Geosciences, Beijing (CUGB). The analytical precisions ( $1\sigma$ ) for  
165 most major elements based on rock standards AGV-2 (US Geological Survey), GSR-1,  
166 GSR-3 and GSR-5 (National geological standard reference materials of China) are better  
167 than 1% with the exception of  $\text{TiO}_2$  (~1.5%) and  $\text{P}_2\text{O}_5$  (~2.0%). Loss on ignition (LOI)  
168 was determined by placing 1 g of samples in the furnace at 1000 °C for several hours  
169 before being cooled in a desiccator and reweighed (Song et al., 2010).

170 The trace element analysis for Kedanshan ultramafic-mafic samples was performed  
171 on an Agilent-7500a inductively coupled plasma mass spectrometer (ICP-MS) in the  
172 Institute of Earth Science of CUGB. About 40 mg of sample powder was dissolved in  
173 equal mixture of subboiling distilled  $\text{HNO}_3$  and HF with a Teflon digesting vessel on a  
174 hotplate at 185 °C for 48 h using high-pressure bombs for digestion/dissolution. The  
175 samples were then evaporated to incipient dryness, refluxed with 6 N  $\text{HNO}_3$ , and heated  
176 again to incipient dryness. The sample was again dissolved in 2 mL of 3 N  $\text{HNO}_3$  in  
177 high-pressure bombs for a further 24 h to ensure complete dissolution. Such digested  
178 samples were diluted with Milli-Q water to a final dilution factor of 2000 in 2%  $\text{HNO}_3$   
179 solution with total dissolved solid of 0.05 %. Precisions ( $1\sigma$ ) for most elements based on  
180 liquid standards Std-1, Std-2, Std-4 (AccuStandard, USA). Rock standards AGV-2 (US  
181 Geological Survey), and GSR-1, GSR-3, GSR-5 (National geological standard reference  
182 materials of China) were used to monitor the analytical accuracy and precision. The

183 analytical accuracy, as indicated by relative difference between measured and  
184 recommended values, is better than 5% for most elements, and 10-15% for Cu, Zn, Gd  
185 and Ta.

### 186 **4.3 Zircon U-Pb geochronology**

187 Zircons were separated from three gabbroic samples (13LX-17, 13LX-18 and  
188 13LX-19) by using standard density and magnetic separation techniques and selected by  
189 handpicking under a binocular microscope. The Cathodoluminescence (CL) examination  
190 was done by using an FEI QUANTA650 FEG Scanning Electron Microscope (SEM)  
191 under conditions of 15 kV/120 nA in the School of Earth and Space Sciences, Peking  
192 University, Beijing.

193 Measurements of U, Th and Pb in zircons were carried out on an Agilent-7500a  
194 quadrupole inductively coupled plasma mass spectrometry coupled with a New Wave SS  
195 UP193 laser sampler (LA-ICP-MS) at CUGB. Laser spot size of 36  $\mu\text{m}$ , laser energy  
196 density of 8.5  $\text{J}/\text{cm}^2$  and a repetition rate of 10 Hz were applied for analysis (see [Song et](#)  
197 [al., 2010](#) for more details). Age calculations and plots of concordia diagrams were done  
198 using Isoplot ([Ludwig, 2003](#)).

## 199 **5 Results**

### 200 **5.1 Mineral chemistry**

#### 201 *5.1.1 Olivine*

202 Because the olivine in all the dunite samples has been altered into serpentine ([Fig.](#)  
203 [3A to C](#)), we cannot see the complete variation of olivine compositions from dunite to

204 pyroxenite. Olivine in pyroxene-peridotite and olivine-bearing pyroxenite shows a  
205 narrow compositional change of forsterite contents (Fo) from 85.3 to 83.4, with NiO  
206 contents vary from 0.03 to 0.23 wt.% (Table S1; Fig. 4A). The olivines are also  
207 characterized by extremely low CaO contents (< 0.14 wt.%), similar to olivines from the  
208 Alaskan type complexes, much lower than olivines from komatiite and picrite (Fig. 4B).

### 209 **5.1.2 Pyroxene**

210 Representative pyroxene compositions of the studied samples are given in Table S2  
211 and shown in a ternary plot of the Wo-En-Fs diagram (Fig. 5A). The clinopyroxenes are  
212 mostly diopsides with subordinate augites, and are Ca-rich with a formula of  
213  $\text{Wo}_{39.2-48.8}\text{En}_{42.9-52.5}\text{Fs}_{4.2-13.7}$ . Their Mg# [ $100 \times \text{Mg}/(\text{Mg} + \text{Fe}^{2+})$ ] varies from 92.1 in the  
214 dunite to 75.7 in gabbro, and is positively correlated with  $\text{Cr}_2\text{O}_3$  (Fig. 5B, Table S2). All  
215 clinopyroxenes in the studied samples are characterized by low  $\text{TiO}_2$  (0-0.53 wt.%),  
216  $\text{Cr}_2\text{O}_3$  (0.04-1.00 wt.%),  $\text{Al}_2\text{O}_3$  (1.11-6.89 wt.%) and  $\text{Na}_2\text{O}$  (0-0.87 wt.%), showing a  
217 narrow compositional range (Table S2). In the Al<sub>2</sub>O<sub>3</sub> versus  $\text{TiO}_2$  wt.% diagram (Fig. 5C),  
218 clinopyroxene compositions plot in the Alaskan-type field and show an arc cumulate  
219 trend. The homogeneous  $\text{TiO}_2$  and  $\text{Al}_2\text{O}_3$ , as well as high CaO, are similar to those from  
220 Alaskan-type intrusions in many places worldwide (Snoke et al. 1981; Helmy and El  
221 Mahallawi, 2003; Farahat and Helmy, 2006; Helmy et al., 2015).

222 Orthopyroxene (Opx) is rare in the Kedanshan ultramafic-mafic intrusion, and its  
223 composition is bronzite with a formula of  $\text{Wo}_{1.4-1.7}\text{En}_{73.9-83.7}\text{Fs}_{14.8-24.4}$  (Fig. 5A).

### 224 **5.1.3 Plagioclase**

225 Representative plagioclase compositions are given in [Table S3](#). Plagioclases in  
226 layered gabbro have homogeneous compositions without chemical zonation. They are  
227 Ca-rich (18.59-20.56 wt.%) with anorthite (An) contents from 91.39 to 98.04 wt.%,  
228 consistent with An contents from Alaskan-type complexes (e.g., [Irvine, 1974](#);  
229 [Himmelberg and Lonely, 1995](#)).

### 230 **5.1.4 Chromian spinel**

231 Chromian spinel occurs as an accessory mineral in dunite and pyroxene peridotite.  
232 Representative analytical data of chromian spinels from these rocks are shown in [Table](#)  
233 [S4](#). They are characterized by low content of TiO<sub>2</sub>, varying contents of Cr<sub>2</sub>O<sub>3</sub>, FeO<sub>T</sub> and  
234 MgO, and a negative correlation between Cr<sub>2</sub>O<sub>3</sub> and MgO contents. Cr# [ $100 \times \text{Cr} / (\text{Cr} + \text{Al})$ ]  
235 values of chromian spinels systematically change from 69.2-40.9 (average, 52.1) in  
236 dunite, 55.8-43.5 in pyroxene peridotite, to 39.0 in olivine pyroxenite. As shown in [Fig. 6](#),  
237 all these chromian spinels have chemical features similar to those from Alaskan-type  
238 complexes ([Snoke et al., 1981](#); [Himmelberg and Loney, 1995](#); [Helmy et al., 2015](#)), but  
239 are distinguishable from spinels from ophiolites, MORB, boninites and abyssal  
240 peridotites.

## 241 **5.2 Whole-rock geochemistry**

242 The major and trace element compositions for representative samples from the  
243 Kedanshan ultramafic-mafic intrusion are listed in [Table 1](#). These samples show wide  
244 compositional variation in both major and trace elements from dunite, pyroxene

245 peridotite, olivine pyroxenite to gabbro. MgO contents are positively correlated with TiO<sub>2</sub>  
246 and Yb in gabbros, but negatively correlated with TiO<sub>2</sub> and Yb in dunites and peridotites  
247 (Fig. 7A and B). All rocks show negative correlations in MgO vs. Al<sub>2</sub>O<sub>3</sub> and CaO (Fig.  
248 7C and D), but have different trends in MgO vs. CaO/Al<sub>2</sub>O<sub>3</sub> in peridotites and gabbros  
249 (Fig. 7E). The compatible elements (Co, Cr and Ni) are positively correlated with MgO  
250 contents (Fig. 7F-H). The positive correlation between Cr and Ni contents (Fig. 7I)  
251 suggests that fractional evolution of magma is firstly controlled by olivine and then by  
252 clinopyroxene. The systematic variations of compositions from dunite to gabbro (Fig.  
253 7A-H) indicate that the Kedanshan ultramafic-mafic intrusion originated from various  
254 degrees of fractional crystallization from an identical magma type (see below).

255 The chondrite-normalized REE and primitive mantle-normalized multi-element  
256 diagrams are shown in Fig. 8. The total of REEs of the studied samples varies from 0.31  
257 ppm in dunite to 5.71 ppm in gabbro. They exhibit significant variation in normalized  
258 element patterns (Fig. 8A). The dunite and peridotite samples display LREE enriched  
259 (U-shaped) patterns with various extent of negative Eu anomaly ( $Eu/Eu^* = 0.20-0.99$ ),  
260 while the olivine pyroxenite and gabbro exhibit LREE depleted patterns  
261 ( $LREE/HREE = 0.73-1.17$ ), with a strongly positive Eu anomaly in gabbroic samples  
262 ( $Eu/Eu^* = 1.30-1.75$ ). In primitive mantle-normalized multi-element diagrams (Fig. 8B),  
263 the studied samples display arc-like patterns characterized by enrichments in LILEs  
264 relative to HFSEs (Gill, 1981; Grove et al., 2003), and have positive anomalies in Ba, U,  
265 Pb and Sr, and various Nb and Ta anomalies. Significant variations of trace elements

266 from dunite to gabbro indicate an obvious process of fractional crystallization. The  
267 positive Eu, Ba and Sr anomalies from gabbro are originated from plagioclase  
268 accumulation (Niu and O'Hara, 2009). The various negative Eu anomalies in ultramafic  
269 rocks indicate the absence of plagioclase in the process of their crystallization, which is  
270 supported by their petrography.

### 271 **5.3 Zircon U-Pb ages**

272 Two samples from cumulate gabbro layers (13LX-17 and 13LX-19) and one gabbro  
273 sample from a vein (13LX-18) were selected for zircon geochronological study. The  
274 results of LA-ICP-MS U-Pb zircon analyses are listed in Table 2. The CL images and  
275 U-Pb concordia diagrams are shown in Fig. 9. Zircons from these gabbro samples are  
276 colorless and exhibit rectangle or irregular shapes with long axes of 50-120  $\mu\text{m}$  and  
277 length/width ratios of 1.1-2.0. The CL images display a feature for zircons of magmatic  
278 origin with straight and wide oscillatory growth band (Fig. 9A).

279 Zircons from sample 13LX-17 have variable contents of U (58-1460 ppm) and Th  
280 (56-743 ppm) with Th/U ratios of 0.11-2.16. Six analyses yield apparent  $^{206}\text{Pb}/^{238}\text{U}$  ages  
281 of 202-188 Ma with a weighted mean of  $193\pm 6$  Ma (MSWD=2.4; Fig. 9B). Four analyses  
282 yield  $^{206}\text{Pb}/^{238}\text{U}$  ages of 299-284 Ma with a weighted mean of  $295\pm 13$  Ma (MSWD=0.26),  
283 other two give apparent  $^{206}\text{Pb}/^{238}\text{U}$  ages of  $406\pm 6$  Ma and  $422\pm 6$  Ma, which would be the  
284 inherited ages of the CAO (e.g., Song et al., 2015). One zircon gives  $1767\pm 25$  Ma,  
285 which is derived from Precambrian basement (Table 2).

286 Zircons from gabbroic vein sample 13LX-18 have variable contents of U (111-1255

287 ppm) and Th (81-1669 ppm) with Th/U ratios of 0.17-1.86. Six analyses yield apparent  
288  $^{206}\text{Pb}/^{238}\text{U}$  ages of 160-153 Ma with a weighted mean of  $156\pm 3$  Ma (MSWD=0.42; Fig.  
289 9C), which is interpreted as the emplacement age of the vein. One analysis give apparent  
290  $^{206}\text{Pb}/^{238}\text{U}$  ages of  $504\pm 7$  Ma, three analyses give a mean age of  $1892\pm 28$  Ma  
291 (MSWD=0.002) and other five from an intercept age of  $1039\pm 50$  Ma (Fig. 9C).

292 Zircons from sample 13LX-19 show highly variable U (49-1469 ppm) and Th  
293 (31-782 ppm) with Th/U ratios of 0.12-2.01. Eight analyses yield apparent  $^{206}\text{Pb}/^{238}\text{U}$   
294 ages of 188-171 Ma with a weighted mean of  $179\pm 4$  Ma (MSWD=1.6; Fig. 9D), which is  
295 interpreted as the formation age of the Kedanshan ultramafic-mafic intrusion. Four  
296 analyses give apparent  $^{206}\text{Pb}/^{238}\text{U}$  ages of 1809-1808 Ma, one give  $1928\pm 25$  Ma and one  
297  $2154\pm 27$  Ma, which are xenocrysts derived from a Paleoproterozoic basement (Table 2).

298 On the basis of zircon analyses from the three gabbroic samples, the Kedanshan  
299 ultramafic-mafic intrusion formed in a long-lasting period of 193-179 Ma in Jurassic time.  
300 Zircon xenocrysts in these samples reveal that they are sourced from (1) a  
301 Paleoproterozoic basement with ages of 2100-1800 Ma associated with assembly of  
302 Columbia Supercontinent, (2) Grenvillian-aged orogeny of ~1000 Ma, and (3) the rocks  
303 of Paleozoic to Triassic ages from the CAOB.

## 304 **6. Discussion**

### 305 **6.1 Petrogenesis: Alaskan-type ultramafic-mafic intrusion vs. ophiolite**

306 Most researchers have considered the Kedanshan ultramafic-mafic intrusion as an  
307 ophiolite, related to the Paleo-Asian Ocean (e.g., Liang, 1994; Li et al., 2011). However,

308 lines of evidence in this study confirm it is an Alaskan-type ultramafic-mafic intrusion,  
309 formed in a super-subduction environment.

310 The Kedanshan ultramafic-mafic intrusion is an accumulated complex comprising  
311 dunite, pyroxene peridotite, olivine pyroxenite and gabbro/anorthosite without pillow  
312 lava and radiolite. Such a rock assemblage is different from all ophiolites of the  
313 Paleo-Asian Ocean in the eastern CAOB (Song et al., 2015). The variable compositions  
314 of olivine, clinopyroxene and chromian spinel show affinities with Alaskan-type  
315 intrusions (Fig. 4 to 6). The Fo values of olivine agree with those from typical  
316 Alaskan-type complexes worldwide (e.g., Irvine, 1976; Himmelberg et al., 1986; Clark,  
317 1980; Rublee, 1994; Helmy and Moggesie, 2001; Pettigrew and Hattori, 2006).

## 318 **6.2 Fractionation and accumulation**

319 The Kedanshan ultramafic-mafic intrusion consists of several lithologies varying  
320 from dunite to gabbro. Increases of Al<sub>2</sub>O<sub>3</sub> and CaO and decreases of compatible elements  
321 (Co, Cr and Ni) from dunite to gabbro indicate a crucial role for  
322 fractionation/accumulation of olivine, spinel, clinopyroxene and Ca-plagioclase (Fig.7).

323 In the AFM diagram (Fig.10), the studied samples plot in the arc-related ultramafic  
324 cumulative field. Samples from dunite show negative Eu and Sr anomalies, indicating  
325 olivine-controlled accumulation. Samples from olivine pyroxenite (e.g., 13LX-20 and  
326 13LX-21) have La<sub>N</sub>/Nd<sub>N</sub> ratios less than 1.0 (N denotes chondrite normalization),  
327 suggesting Cpx-controlled accumulation (Guo et al., 2007). The gabbro samples display  
328 positive Eu and Sr anomalies, favoring Pl-controlled accumulation (Fig.8).



### 329 **6.3 Nature of parental magma**

330 In terms of field observations and petrography (Fig. 2 and 3), the crystallization  
331 sequences of minerals can be determined as olivine → chromian spinel → pyroxene →  
332 plagioclase, indicating that the parental magma of the Kedanshan ultramafic-mafic  
333 intrusion is hydrous (Gaetani, 1993). The early formed Mg-rich olivine and chromian  
334 spinel can be used to estimate the parental melt composition in equilibrium with the  
335 Kedanshan ultramafic-mafic intrusion. We use the equation of Maurel and Maurel (1982)  
336 to calculate Al<sub>2</sub>O<sub>3</sub> contents of the parental melt:  $(\text{Al}_2\text{O}_3)_{\text{spinel}} = 0.035 \times (\text{Al}_2\text{O}_3)_{\text{melt}}^{2.42}$ . The  
337 FeO/MgO ratios of the parental melt are calculated by the equation of Roeder and Emslie  
338 (1970):  $K_D = (\text{FeO/MgO})_{\text{olivine}} / (\text{FeO/MgO})_{\text{melt}}$ , where the value of partition coefficient  
339  $K_D$  is 0.30±0.03. The TiO<sub>2</sub> contents of the parental melt are calculated by the equation of  
340 Rollinson (2008):  $(\text{TiO}_2)_{\text{melt}} = 1.0963 \times (\text{TiO}_2)_{\text{spinel}}^{0.7863}$ .

341 Due to fractionation/accumulation, the MgO/FeO ratios calculated from olivine in  
342 pyroxene peridotite and olivine pyroxenite require the parental melt to be high-Mg with  
343 Mg# more than 64.1 (Table S1). The calculated Al<sub>2</sub>O<sub>3</sub> and TiO<sub>2</sub> contents of the parental  
344 melt are 12.19-16.58 wt.% and 0.15-0.41 wt.%, respectively (Table S4). These  
345 calculations illustrate that the parental melt in equilibrium with the Kedanshan  
346 ultramafic-mafic intrusion is rich in Al and Mg and poor in Ti.

347 On the other hand, the high Cr<sub>2</sub>O<sub>3</sub> and Wo contents of clinopyroxene, as well as high  
348 NiO and Fo from olivine, show these minerals crystallized in a hydrous basaltic magma  
349 system (Sisson and Grove, 1993; Eyuboglu et al., 2010). In addition, Al-rich chromian

350 spinel and An-rich plagioclase indicate that the liquidus composition was high in H<sub>2</sub>O  
 351 and Ca (Sisson and Grove, 1993; Cleason and Meurer, 2004), suggesting that the parental  
 352 magma was relatively rich in Al, Mg, Ca and H<sub>2</sub>O, and low in Ti.

353 The Kedanshan ultramafic-mafic intrusion show variable effects of crystal  
 354 accumulation, so the whole-rock geochemistry can't represent the parental magma  
 355 composition; instead it equals the sum of composition of the accumulative crystals and  
 356 trapped melts (Bédard, 1994). In the following parts, we use the method of proposed by  
 357 Guo et al. (2015) to estimate the parental magma composition of the Kedanshan  
 358 ultramafic-mafic intrusion. Making by using olivine, the calculated formula can be  
 359 expressed as:

$$\begin{cases} c_i^{rock} = \varphi^{Ol} c_i^{Ol} + \varphi^{Cpx} c_i^{Cpx} + \varphi^{Opx} c_i^{Opx} + \varphi^{TM} c_i^{TM} ; \\ \frac{c_i^{Ol}}{c_i^{Cpx}} = \frac{D_i^{Ol/Melt}}{D_i^{Cpx/Melt}}, \frac{c_i^{Ol}}{c_i^{Opx}} = \frac{D_i^{Ol/Melt}}{D_i^{Opx/Melt}}, \frac{c_i^{Ol}}{c_i^{TM}} = D_i^{Ol/Melt} ; \end{cases}$$

360

$$\Rightarrow c_i^{Ol} = \frac{c_i^{rock}}{\varphi^{Ol} + \varphi^{Cpx} \frac{D_i^{Cpx/Melt}}{D_i^{Ol/Melt}} + \varphi^{Opx} \frac{D_i^{Opx/Melt}}{D_i^{Ol/Melt}} + \varphi^{TM} \frac{1}{D_i^{Ol/Melt}}}$$

361 To simplify the calculation, the Kedanshan ultramafic-mafic intrusion is reduced to  
 362 less than three-phase assemblages with a hypothetical trapped melt of 0-15 vol.%. The  
 363 detailed calculation results with different trapped melts for studied samples are given in  
 364 Table S5. The modal mineral compositions ( $\varphi$ ) of the studied samples and partition  
 365 coefficients (D) used in the calculation are given in Table S6 and S7, respectively. Here,  
 366 we select the four samples (13LX-28, 11, 12 and 21) to estimate the composition of the  
 367 parental magmas in equilibrium with the Kedanshan ultramafic-mafic intrusion. As

368 shown in [Fig.11](#), the calculated parental magmas for every sample and different trapped  
369 melt fraction are enriched in LILEs, Th-U and LREEs, and depleted in Nb-Ta. These  
370 features suggest that the parental magmas of the Kedanshan ultramafic-mafic intrusion  
371 have arc geochemical affinities.

#### 372 **6.4 Long-lived superimposed subduction of the Mongol-Okhotsk and** 373 **Paleo-Pacific oceans**

374 Petrology and chemical composition of Kedanshan ultramafic-mafic intrusion  
375 suggests that the magma generation was in a subduction-related setting. The Cpx  
376 compositions also show geochemical affinities with arc basalts of a subduction-related  
377 setting ([Fig. 12](#)).

378 The studied region is located in the central Inner Mongolia region of the  
379 southeastern segment of the CAOB, which experienced Paleozoic orogeny by closure of  
380 the Paleo-Asian Ocean from Early Paleozoic to Triassic ([Miao et al., 2007, 2008; Jian et](#)  
381 [al., 2012; Xu et al., 2013b, 2015; Song et al., 2015](#)). To the east is the Mesozoic tectonism  
382 of the Paleo-Pacific Ocean that started to subduct westwards at ~200-190 Ma (e.g.,  
383 [Zhou et al., 2009; Wu et al., 2011; Zhou and Wilde, 2013](#)), and to the north is the  
384 Mesozoic tectonism of the Mongol-Okhotsk Ocean ([Zonenshain et al., 1990; Zorin, 1999;](#)  
385 [Tang et al., 2014; Wang et al., 2011, 2012, 2015a](#)). However, the influence of these  
386 Mesozoic orogenies on the Kedanshan region remains equivocal, although some recent  
387 researches have supplied important perspectives (e.g., [Xu et al., 2013a; Wang et al.,](#)  
388 [2015a](#)).

389 The final closure of the Paleo-Asian Ocean was proposed to be finished in the  
390 Triassic (>220 Ma) along the E-N-trending Solonker-Xar Moron suture zone (e.g., [Jian et](#)  
391 [al., 2012](#); [Cao et al., 2013](#); [Xu et al., 2013b, 2015](#); [Zhao et al., 2014](#); [Song et al., 2015](#)). It  
392 means that the formation time of the Kedanshan ultramafic-mafic intrusion postdates the  
393 Paleo-Asian Ocean. That is, subduction of the Paleo-Asian Ocean was not responsible for  
394 formation of the Kedanshan complex.

395 As an embayment of the Paleo-Pacific Ocean, the Mongol-Okhotsk Ocean existed in  
396 the Paleozoic to Early Mesozoic between the Central Mongolia Massif and the Siberian  
397 Craton ([Zorin, 1999](#); [Donskaya et al., 2013](#)). Although the closure time of the  
398 Mongol-Okhotsk Ocean is still under debate, the subduction of the Mongol-Okhotsk  
399 Oceanic plate in the Late Paleozoic to Early Mesozoic has been confirmed ([Donskaya et](#)  
400 [al., 2013](#)). [Zorin \(1999\)](#) suggested that the complete closure of the western part of the  
401 Mongol-Okhotsk Ocean occurred in the Early to Middle Jurassic. In the eastern side of  
402 the Mongol-Okhotsk tectonic belt, several early Mesozoic porphyry-type deposits  
403 outcrop in the Chinese border area ([Fig. 1A](#)), such as the Taipingchuan porphyry Cu-Mo  
404 deposit (~202 Ma, [Chen et al., 2010](#)), the Wunugetushan porphyry Cu-Mo deposit  
405 (183-178 Ma, [Chen et al., 2011](#)) and the Badaguan porphyry Cu-Mo deposit (188-182 Ma,  
406 [Shen et al., 2010](#)). These porphyry-type deposits are thought to result from subduction of  
407 the Mongol-Okhotsk Ocean (e.g., [Tang et al., 2014](#)). In addition, some Early Mesozoic  
408 granitoids related to subduction of the Mongol-Okhotsk Oceanic plate have been reported  
409 along both sides of the eastern Mongol-Okhotsk orogenic belt ([Orolmaa et al., 2008](#);

410 [Jiang et al., 2010](#); [Liu et al., 2010](#); [Tang et al., 2014](#)). The ocean appears to have closed as  
411 a result of two subduction zones, dipping outwards under both adjacent continental  
412 margins.

413 Paleomagnetic studies show that the Mongol-Okhotsk Ocean had not closed, and its  
414 subduction still took place by ~155 Ma ([Ren et al., 2016](#)). Thus, with respect to the  
415 spatial and temporal relations, we suggest that the Kedanshan ultramafic-mafic intrusion  
416 might be long affected by the far-field effects of the southeastward subduction of the  
417 Mongol-Okhotsk Ocean, during much of the Mesozoic.

418 Separate to the Mongol-Okhotsk Ocean, a S-N-trending accretionary belt with  
419 ophiolites, high-pressure rocks and igneous rocks (210-150 Ma) has been reported in NE  
420 China ([Wu et al., 2005, 2011](#); [Yu et al., 2012](#); [Zhou and Wilde, 2013](#); [Xu et al., 2013a](#); [Li  
421 et al., 2014](#); [Zhou et al., 2009, 2014](#); [Wang et al., 2015b](#); [Guo et al., 2015](#); [Niu et al.,  
422 2015](#)). These rocks suggest westward subduction of the Paleo-Pacific Oceanic plate  
423 during the Mesozoic. Therefore, we suggest that the Paleo-Pacific subduction was also  
424 responsible for formation of the Kedanshan ultramafic-mafic intrusion.

425 Taking these aspects into consideration, we consider that the plate between the  
426 Mongol-Okhotsk Ocean and Paleo-Pacific Ocean ([Fig. 13A](#)) was affected by long-lived,  
427 superimposed subduction during a long part of the Mesozoic (193-179 Ma). The  
428 Mongol-Okhotsk Oceanic plate subducted toward the southeast beneath the Central  
429 Mongolia Massif, and the Paleo-Pacific Oceanic plate subducted toward the northwest  
430 beneath the Central Mongolia Massif in the same time. The long-lived superimposed

431 subduction (Fig. 13B) would form a large, triangle-shaped mantle wedge beneath Central  
432 Mongolia during the Mesozoic (193-179 Ma). Fluids/melts dehydrated from the  
433 subducted oceanic plate could remodify the overlying mantle wedge, and melting of the  
434 large mantle wedge produced hydrous ultramafic-mafic magmas along the superimposed  
435 subduction zones, recorded by the Kedanshan ultramafic-mafic intrusion.

## 436 **7. Conclusions**

437 (1) The Kedanshan ultramafic-mafic intrusion is a cumulate complex, similar to the  
438 Alaskan-type intrusions generated in arc settings.

439 (2) LA-ICP-MS zircon U-Pb data indicate that the ultramafic-mafic intrusion was  
440 formed in Jurassic times with an emplacement age between 193 to 179 Ma.

441 (3) The parental magmas for these Jurassic ultramafic-mafic rocks could be high-Mg,  
442 Al-rich and hydrous basaltic magma, originated from the partial melting of a depleted  
443 mantle wedge that was metasomatized by subduction zone fluids/melts.

444 (4) The formation of the Kedanshan ultramafic-mafic intrusion resulted from  
445 superimposed subduction between the Mongol-Okhotsk and the Paleo-Pacific oceanic  
446 plates during the Mesozoic.

## 447 **Acknowledgements**

448 We thank the staffs of the Geological Lab Center, China University of Geosciences,  
449 Beijing (CUGB), for their helps with major and trace element analyses, and zircon U-Pb  
450 dating. We thank Feng Guo, an anonymous reviewer and Editor-in-chief Mei-Fu Zhou for  
451 their constructive official review comments, which led to a better presentation of the final

452 product. This work was financially supported by the National Key Basic Research  
453 Program of China (2013CB429806) and the National Natural Science Foundation of  
454 China (grants 41572040, 41372060).

## 455 **References**

456 Barnes, S.J., Röeder, P.L., 2001. The range of spinel compositions in terrestrial mafic and  
457 ultramafic rocks. *J. Petrol.* 42, 2279-2302.

458 Beard, J.S., 1986. Characteristic mineralogy of arc-related cumulate gabbros:  
459 implications for the tectonic setting of gabbroic plutons and for andesite genesis.  
460 *Geology* 14, 848-851.

461 Burns L.E., 1985. The Border Ranges ultramafic and mafic complex, south-central  
462 Alaska: cumulate fractionates of island-arc volcanics. *Can. J. Earth Sci.* 22(7),  
463 1020-1038.

464 Bédard, J.H., 1994. A procedure for calculating the equilibrium distribution of trace  
465 elements among the minerals of cumulate rocks, and the concentration of trace  
466 elements in the coexisting liquids. *Chem. Geol.* 118, 143-153.

467 Cao, H.H., Xu, W.L., Pei, F.P., Wang, Z.W., Wang, F., Wang, Z.J., 2013. Zircon U-Pb  
468 geochronology and petrogenesis of the Late Paleozoic-Early Mesozoic intrusive  
469 rocks in the eastern segment of the northern margin of the North China Block.  
470 *Lithos* 170-171, 191-207.

471 Chen, Z.G., Zhang, L.C., Lu, B.Z., Li, Z.L., Wu, H.Y., Xiang, P., Huang, S.W., 2010.  
472 Geochronology and geochemistry of the Taipingchuan copper-molybdenum deposit

473 in Inner Mongolia, and its geological significances. *Acta Petrol. Sin.* 26,1437-1449  
474 (in Chinese with English abstract).

475 Chen, Z.G., Zhang, L.C., Wan, B., Wu, H.Y., Cleven, N., 2011. Geochronology and  
476 geochemistry of the Wunugetushan porphyry Cu-Mo deposit in NE China, and their  
477 geological significance. *Ore Geol. Rev.* 43, 92-105.

478 Cheng, Y.H., Teng, X.J., Li, Y.F., Li, M., Zhang, T.F., 2014. Early Permian East-Ujimqin  
479 mafic-ultramafic and granitic rocks from the Xing'an-Mongolian Orogenic belt,  
480 north china: origin, chronology, and tectonic implications. *J. Asian Earth Sci.* 96,  
481 361-373.

482 Clark, T., 1980. Petrology of the Turnagain ultramafic complex, northwestern British  
483 Colombia. *Can. J. Earth Sci.* 17, 744-757.

484 Cleason, D.T., Meurer, W.P., 2004. Fractional crystallization of hydrous basaltic 'arctype'  
485 magmas and the formation of amphibole-bearing gabbroic cumulates. *Contrib.*  
486 *Mineral. Petrol.* 147, 288-304.

487 Cogné, J.P., Kravchinsky, V.A., Halim, N., Hankard, F., 2005. Late Jurassic-Early  
488 Cretaceous closure of the Mongol-Okhotsk Ocean demonstrated by new Mesozoic  
489 palaeomagnetic results from the Trans-Baikal area (SE Siberia). *Geophysical J.*  
490 *Royal Astronomical Soc.* 163 (3), 813-832.

491 Conrad, W.K., Kay, R.W., 1984. Ultramafic and mafic inclusions from Adak island,  
492 crystallization history, and implications for the nature of primary magmas and  
493 crustal evolution in the Aleutian arc. *J. Petrol.* 25, 88-125.



494 DeBari, S.M., Coleman, R.G., 1989. Examination of the deep levels of an island arc:  
495 evidence from the tonsina ultramafic-mafic assemblage, Tonsina, Alaska. *J. Geophys.*  
496 *Res.* 94, 4373-4391.

497 DeBari, S.M., Kay, S.M., Kay, R.W., 1987. Ultramafic xenoliths from Adagdak volcano,  
498 Adak, Aleutian Islands, Alaska: deformed igneous Cumulates from the Moho of an  
499 Island Arc. *J. Geol.* 95, 329-341.

500 Dick, H.J.B., Bullen, T., 1984. Chromian spinel as a petrogenetic indicator in abyssal and  
501 alpine-type peridotites and spatially associated lavas. *Contrib. Mineral. Petrol.* 86,  
502 54-76.

503 Donskaya, T.V., Gladkochub, D.P., Mazukabzov, A.M., Ivanov, A.V., 2013. Late  
504 paleozoic -mesozoic subduction-related magmatism at the southern margin of the  
505 siberian continent and the 150 million-year history of the mongol-okhotsk ocean. *J.*  
506 *Asian Earth Sci.* 62, 79-97.

507 Eyuboglu, Y., Dilek, Y., Bozkurt, E., Bektaş, O., Rojay, B., Şen, C., 2010. Structure and  
508 geochemistry of an Alaskan-type ultramafic-mafic complex in the eastern Pontides,  
509 NE Turkey. In: Santosh, M., Maruyama, S. (Eds.), *A Tribute to Akiho Miyashiro:*  
510 *Gondwana Res.* 18, 230-252.

511 Farahat, E.S., Helmy, H.M., 2006. Abu Hamamid Neoproterozoic Alaskan-type  
512 complex, south Eastern Desert, Egypt. *J. Afr. Earth Sci.* 45, 187-197.

513 Gaetani, G.A., Grove, T.L., Bryan, W.B., 1993. The influence of water on the  
514 petrogenesis of subduction-related igneous rocks. *Nature* 365, 332-334.

515 Gill, J.B., 1981. *Orogenic Andesites and Plate Tectonics*. Springer Verlag, New York, p.  
516 385.

517 Grove, T.L., Elkins Tanton, L.T., Parman, S.W., Carterjee, N., Muntener, O., Gaetani,  
518 G.A., 2003. Fractional crystallization and mantle melting controls on calc-alkaline  
519 differ-entiation trends. *Contrib. Mineral. Petrol.* 145, 515-533.

520 Guo, F., Li, H.X., Fan, W.M., Li, J.Y., Zhao, L., Huang, M.W., 2016. Variable sediment  
521 flux in generation of Permian subduction-related mafic intrusions from the Yanbian  
522 region, NE China. *Lithos* 261, 195-215.

523 Guo, F., Li, H.X., Fan, W.M., Li, J.Y., Zhao, L., Huang, M.W., Xu, W.L., 2015. Early  
524 Jurassic subduction of the Paleo-Pacific Ocean in NE China: Petrologic and  
525 geochemical evidence from the Tumen mafic intrusive complex. *Lithos* 224-225,  
526 46-60.

527 Guo, F., Nakamura, E., Fan, W.M., Kobayoshi, K., Li, C.W., 2007. Generation of  
528 Palaeocene adakitic andesites by magma mixing; Yanji Area, NE China. *J. Petrol.* 48,  
529 661-692.

530 Helmy, H.M., El Mahallawi, M.M., 2003. Gabbro Akarem mafic-ultramafic  
531 complex, Eastern Desert, Egypt: a late Precambrian analogue of Alaskan-type  
532 complexes. *Mineral. Petrol.* 77, 85-108.

533 Helmy, H.M., Moggesie, A., 2001. Gabbro Akarem, Eastern Desert, Egypt: Cu-Ni-PGE  
534 mineralization in a concentrically zoned mafic-ultramafic complex. *Miner. Deposita*  
535 36, 58-71.

536 Helmy, H.M., Yoshikawa, M., Shibata, T., Arai, S., Kagami, H., 2015. Sm-Nd and Rb-Sr  
537 isotope geochemistry and petrology of Abu Hamamid intrusion, Eastern Desert,  
538 Egypt: an Alaskan-type complex in a back arc setting. *Precambrian Res.* 258,  
539 234-246.

540 Himmelberg, G.R., Loney, R.A., 1995. Characteristics and petrogenesis of Alaskan-type  
541 ultramafic-mafic intrusions, Southeastern Alaska. US Geological Survey  
542 Professional Paper.

543 Himmelberg, R.G., Loney, R.A., Craig, J.T., 1986. Petrogenesis of the ultramafic  
544 complex at the Blashke Islands, southeastern Alaska. U.S. Geological Survey  
545 Bulletin 1662, 1-14.

546 Irvine, T.N., 1967. Chromian spinel as a petrogenetic indicator: part 2. Petrologic  
547 applications. *Can. J. Earth Sci.* 4, 71-103.

548 Irvine, T.N., 1974. Petrology of the Duke Island ultramafic complex southern Alaska.  
549 *Geological Society of Am. Mineral.* 138, 240.

550 Irvine, T.N., 1976. Alaskan-type Ultramafic-gabbro Bodies in the Aiken Lake, McConnel  
551 Creek, and Toodagoone Map-areas. *Geological Survey of Canada Paper* 76-1A pp.  
552 76-81.

553 Ishiwatari, A., Ichiyama, Y., 2004. Alaskan-type plutons and ultramafic lavas in Far East  
554 Russia, Northeast China, and Japan. *International Geolo. Rev.* 46, 316-331.

555 Jian, P., Kröner, A., Windley, B.F., Shi, Y., Zhang, W., Zhang, L., Yang, W., 2012.  
556 Carboniferous and Cretaceous mafic-ultramafic massifs in Inner Mongolia (China):

557 A SHRIMP zircon and geochemical study of the previously presumed integral  
558 “Hegenshan ophiolite”, *Lithos* 142-143, 48-66.

559 Jiang, S.H., Nie, F.J., Su, Y.J., Bai, D.M., Liu, Y.F., 2010. Geochronology and Origin of  
560 the Erdenet Superlarge Cu-Mo Deposit in Mongolia. *Acta Petrol. Sin.* 31, 289-306  
561 (in Chinese with English abstract).

562 Kamenetsky V.S., Gurenko A.A., Kerr A.C., 2010. Composition and temperature of  
563 komatiite melts from Gorgona Island, Colombia, constrained from olivine-hosted  
564 melt inclusions. *Geology* 38(11):1003-1006.

565 KePezhinskas, P., Mcdermott, F., Defant, M. J., Hochstaedter, A., Drummond, M. S.,  
566 Hawkesworth, C. J., Koloskov, A., Maury, R.C., Bellon, H., 1997. Trace element  
567 and Sr-Nd-Pb isotopic constraints on a three-component model of kamchatka arc  
568 petrogenesis. *Geochim. Cosmochim. Acta* 61, 577-600.

569 Kim, N.K., Choi, S.H. 2016. Petrogenesis of late Triassic ultramafic rocks from the  
570 Andong ultramafic complex, South Korea. *Lithos* 264, 28-40.

571 Krause J., Brüggemann G.E., Pushkarev E.V., 2007. Accessory and rock forming minerals  
572 monitoring the evolution of zoned mafic-ultramafic complexes in the Central Ural  
573 Mountains. *Lithos* 95:19-42.

574 Le Bas, M.J., 1962. The role of aluminum in igneous clinopyroxenes with relation to their  
575 parentage. *Am. J. Sci.* 260, 267-288.

576 Li, H., Liu, Q., Hou, Q.L., Xu, H.H., Zhu, M.X., Zeng, G.H., 2011. Distribution and  
577 fractionation of Platinum-group elements in mantle peridotites from Kedanshan

578 ophiolite, Inner Mongolia. *Acta Petrol. Sin.* 27, 1759-1769 (in Chinese with English  
579 abstract).

580 Li, J.Y., Guo, F., Li, C.W., Li, H.X., Zhao, L., 2014. Neodymium isotopic variations of  
581 Late Paleozoic to Mesozoic I- and A-type granitoids in NE China: implications for  
582 tectonic evolution. *Acta Petrol. Sin.* 30, 1995-2008 (in Chinese with English  
583 abstract).

584 Li, S., Wang, T., Tong, Y., 2010. Spatial-temporal distribution and tectonic settings of  
585 Early Mesozoic granitoids in the middle-south segment of the Central Asia Orogenic  
586 System. *Acta Petrol. Mineral.* 29 (6), 642-662 (in Chinese with English abstract).

587 Li, Y.J., Wang, J.F., Dong, P.P., Liu, Y.C., Liu, D.W., Bai, H., 2012a. Recognition of  
588 diyanmiao ophiolite in xi u jimqin banner, inner mongolia. *Acta Petrol. Sin.* 28,  
589 1282-1290 (in Chinese with English abstract).

590 Li, C., Thakurta, J., Ripley, E.M., 2012b. Low-Ca contents and kink-banded textures are  
591 not unique to mantle olivine: evidence from the Duke Island Complex, Alaska.  
592 *Mineral. Petrol.* 104(3):147-153.

593 Liang, R.X., 1994. The features of ophiolites in the central sector of Inner Mongolia and  
594 its geological significance. *Regional Geology of China* 1, 37-45 (in Chinese with  
595 English abstract).

596 Liu, Y.F., Nie, F.J., Jiang, S.H., Xue, J., Hou, W.R., Yun, F., 2010. The Geochronology  
597 and Geochemical Features of Ore-hosting Granite in the Aryn nuur Molybdenum  
598 Deposit, Mongolia. *Acta Geosci. Sin.* 31 (03), 343-349 (in Chinese with English

599 abstract).

600 Loucks, R.R., 1990. Discrimination of ophiolitic from nonophiolitic ultramafic-mafic  
601 allochthons in orogenic belts by the Al/Ti ratio in clinopyroxene. *Geology* 18,  
602 346-349.

603 Ludwig, K.R., 2003. User's manual for Isoplot 3.00: a geochronological toolkit for  
604 Microsoft Excel (No. 4). Kenneth R. Ludwig.

605 Maurel, C., Maurel, P., 1982. Étude expérimentale de la distribution de l'aluminium entre  
606 bain silicaté basique et spinelle chromifère. Implications pétrogénétiques: teneur  
607 en chrome des spinelles. *Bull. Minéral.* 105, 197-202.

608 Meibom, A., Sleep, N.H., Chamberlain, C.P., Coleman, R.G., Frel, R., Hren, M.T.,  
609 Wooden, J.L., 2002. Re-Os isotopic evidence for long-lived heterogeneity and  
610 equilibration processes in the Earth's upper mantle. *Nature* 419, 705-708.

611 Miao, L., Zhang, F., Fan, W.M., Liu, D., 2007. Phanerozoic evolution of the Inner  
612 Mongolia Daxinganling orogenic belt in North China: constraints from  
613 geochronology of ophiolites and associated formations. Geological Society London  
614 Special Publications 280, 223-237.

615 Miao, L.C., Fan, W.M., Liu, D.Y., Guo, F., 2008. Geochronology and geochemistry of the  
616 Hegenshan ophiolitic complex: Implications for late-stage tectonic evolution of the  
617 Inner Mongolia-Daxinganling Orogenic Belt, China. *J. Asian Earth Sci.* 32, 348-370.

618 Morimoto, N., 1988. Nomenclature of Pyroxenes. *Mineral. Petrol.* 39, 55-76.

619 Murray, C.G., 1972. Zoned ultramafic complexes of the Alaskan type: feeder pipes of

620 andesitic volcanoes. In: Shagam, R.E., et al. (Eds.). Studies in Earth and Space  
621 Science (Hess Volume), Geologic Society of America Memoir, vol. 132, pp.  
622 313-335.

623 Niu, Y.L., Gilmore, T., Mackie, S., Greig, A., Bach, W., 2002. Mineral chemistry,  
624 wholerock compositions and petrogenesis of ODP Leg 176 gabbros: data and  
625 discussion. In: Natland, J.H., Dick, H.J.B., Miller, D.J., Von Herzen, R.P. (Eds.),  
626 Proc. ODP: Sci. Results, vol. 176 1-60 pp.

627 Niu, Y.L., Liu, Y., Xue, Q.Q., Shao, F.L., Chen, S., Duan, M., et al., 2015. Exotic origin  
628 of the Chinese continental shelf: new insights into the tectonic evolution of the  
629 western Pacific and eastern China since the Mesozoic. *Sci. Bull.* 60(18):1598-1616.

630 Niu, Y.L., O'Hara, M.J., 2009. MORB mantle hosts the missing Eu (Sr, Nb, Ta and Ti) in  
631 the continental crust: New perspectives on crustal growth, crust–mantle  
632 differentiation and chemical structure of oceanic upper mantle. *Lithos* 112, 1-17.

633 Orolmaa, D., Erdenesaihan, G., Borisenko, A.S., Fedoseev, G.S., Babich, V.V., Zhmodik,  
634 S.M., 2008. Permian-Triassic granitoid magmatism and metallogeny of the Hangayn  
635 (central Mongolia). *Rus. Geolo. Geophys.* 49, 534-544.

636 Pettigrew, N.T., Hattori, K.H., 2006. The Quetico Intrusions of Western Superior  
637 Province: Neo-Archean examples of Alaskan/Ural-type mafic-ultramafic intrusions.  
638 *Precambrian Res.* 149, 21-42.

639 Polat, A., Appel, P.W.U., Fryer, B.J., 2011. An overview of the geochemistry of  
640 Eoarchean to Mesarchean ultramafic to mafic volcanic rocks, SW Greenland:

641 Implications for mantle depletion and petrogenetic processes at subduction zones in  
642 the early Earth. *Gondwana Res.* 20, 255-283.

643 Ren, Q., Zhang, S.H., Wu, H.C., Liang, Z.K., Miao, X.J., Zhao, H.Q., Li, H.Y., Yang,  
644 T.S., Pei, J.L., Davis, G.A., 2016. Further paleomagnetic results from the ~ 155 Ma  
645 Tiaojishan Formation, Yanshan Belt, North China, and their implications for the  
646 tectonic evolution of the Mongol-Okhotsk suture. *Gondwana Res.* 35:180-191.

647 Ripley, E.M., 2009. Magmatic sulfide mineralization in Alaskan-type complexes. In: Li,  
648 C.S., Ripley, E.M. (Eds.), *New Development in Magmatic Ni-Cu and PGE Deposits*  
649 7. Geological Publishing House, Beijing, pp. 219-228.

650 Roeder, P.L., Emslie, R.F., 1970. Olivine-liquid equilibrium. *Contrib. Mineral. Petrol.* 29,  
651 275-289.

652 Rollinson, H., 2008. The geochemistry of mantle chromitites from the northern part of the  
653 Oman ophiolite: inferred parental melt compositions. *Contrib. Mineral. Petrol.* 156,  
654 273-288.

655 Rublee, V.J., 1994. *Chemical Petrology, Mineralogy and Structure of the Tulameen*  
656 *Complex, Princeton Area, British Columbia. Unpublished M.Sc. Thesis. University*  
657 *of Ottawa, Canada, p. 179.*

658 Shen, C.L., Zhang, M., Yu, X.Q., Chen, W.G., Gao, W.Y., Zhou, W.C., 2010. New  
659 progresses in exploration of molybdenum deposits and analysis of mineralization  
660 prospect in Inner Mongolia. *Geolo. Explor.* 46, 561-575 (in Chinese with English  
661 Abstract).



662 Sisson, T.W., Grove, T.L., 1993. Experimental investigations of the role of H<sub>2</sub>O in  
663 calcalkaline differentiation and subduction zone magmatism. *Contrib. Mineral.*  
664 *Petrol.* 113, 143-166.

665 Snoke, A.W., Quick, J.E., Bowman, H.R., 1981. Bear mountain igneous complex,  
666 Klamath mountains, California: an ultrabasic to silicic calc-alkaline suite. *J. Petrol.*  
667 22, 501-552.

668 Song, S.G., Niu, Y.L., Wei, C.J., Ji, J.Q., Su, L., 2010. Metamorphism, anatexis, zircon  
669 ages and tectonic evolution of the Gongshan block in the northern Indochina  
670 continent-an eastern extension of the Lhasa Block. *Lithos* 120, 327-346.

671 Song, S.G., Wang, M.M., Xu, X., Wang, C., Niu, Y.L., Allen, M.B., Su, L., 2015.  
672 Ophiolites in the Xing'an-Inner Mongolia accretionary belt of the CAOB:  
673 Implications for two cycles of seafloor spreading and accretionary orogenic events.  
674 *Tectonics* 34, 2221-2245.

675 Sorokin, A.A., Yarmolyuk, V.V., Kotov, A.B., 2004. Geochronology of Triassic-Jurassic  
676 granitoids in the southern framing of the Mongol-Okhotsk foldbelt and the problem  
677 of Early Mesozoic granite formation in Central and Eastern Asia. *Dokl. Earth Sci.*  
678 399, 1091-1094.

679 Su, B.X., Qin, K.Z., M., Santosh., Sun, H., Tang, D.M., 2013. The Early Permian  
680 mafic-ultramafic complexes in the Beishan Terrane, NW china: Alaskan-type  
681 intrusives or rift cumulates? *J. Asian Earth Sci.* 66, 175-187.

682 Sun, S.S., McDonough, W.F., 1989. Chemical and isotopic systematics of oceanic basalts;

683 implications for mantle composition and processes. Geological Society London  
684 Special Publications 42, 313-345.

685 Tang, J., Xu, W.L., Wang, F., Wang, W., Xu, M.J., Zhang, Y.H., 2014. Geochronology and  
686 geochemistry of Early-Middle Triassic magmatism in the Erguna Massif, NE China:  
687 constraints on the tectonic evolution of the Mongol-Okhotsk Ocean. *Lithos* 184-187,  
688 1-16.

689 Thakurta, J., Ripley, E.M., Li, C., 2008. Geochemical constraints on the origin of sulfide  
690 mineralization in the Duke Island Complex, southeastern Alaska. *Geochem.*  
691 *Geophys. Geosys.* 9, 3562-3585.

692 Tistl, M., Burgath, K.P., Hohndorf, A., Kreuzer, H., Munoz, R., Salinas, R., 1994. Origin  
693 and emplacement of Tertiary ultramafic complexes in northwest Colombia:  
694 Evidence from geochemistry and K-Ar, Sm-Nd and Rb-Sr isotopes. *Earth Planet.*  
695 *Sci. Lett.* 126, 41-59.

696 Tong, Y., Hong, D.W., Wang, T., Shi, X.J., Zhang, J.J., Zeng, T., 2010. Spatial and  
697 temporal distribution of granitoids in the middle segment of the Sino-Mongolian  
698 Border and its tectonic and metallogenic implications. *Acta Geosci. Sin.* 31, 395-412  
699 (in Chinese with English abstract).

700 Wang, F., Xu, W.L., Xu, Y.G., Gao, F.H., Ge, W.C., 2015b. Late Triassic bimodal igneous  
701 rocks in eastern Heilongjiang Province, NE China: implications for the initiation of  
702 subduction of the Paleo-Pacific Plate beneath Eurasia. *J. Asian Earth Sci.* 97,  
703 406-423.

- 704 Wang, T., Guo, L., Zhang, L., Yang, Q.D., Zhang, J.J., Tong, Y., Ye, K., 2015a. Timing  
705 and evolution of Jurassic-Cretaceous granitoid magmatisms in the Mongol-Okhotsk  
706 belt and adjacent areas, NE Asia: Implications for transition from contractional  
707 crustal thickening to extensional thinning and geodynamic settings. *J. Asian Earth*  
708 *Sci.* 97, 365-392.
- 709 Wang, T., Guo, L., Zheng, Y.D., Donskaya, T., Gladkochub, D., Zeng, I.S., 2012. Timing  
710 and processes of late Mesozoic mid-lower-crustal extension in continental NE Asia  
711 and implications for the tectonic setting of the destruction of the North China Craton:  
712 mainly constrained by zircon U-Pb ages from metamorphic core complexes. *Lithos*  
713 154, 315-345.
- 714 Wang, T., Zheng, Y.D., Zhang, J.J., Zeng, I.S., Donskaya, T., Guo, L., Li, J.B., 2011.  
715 Pattern and kinematic polarity of late Mesozoic extension in continental NE Asia:  
716 perspectives from metamorphic core complexes. *Tectonics* 30 (6), TC6007,  
717 doi:10.1029/2011TC002896.
- 718 Wu, F.Y., Yang, J.H., Wilde, S.A., Zhang, X.O., 2005. Geochronology, petrogenesis and  
719 tectonic implications of Jurassic granites in the Liaodong Peninsula, NE China,  
720 *Chem. Geol.* 221,127-156.
- 721 Wu, F.Y., Sun, D.Y., Ge, W.C., Zhang, Y.B., Grant, M.L., Wilde, S.A., Jahn, B.M., 2011.  
722 Geochronology of the Phanerozoic granitoids in northeastern China. *J. Asian Earth*  
723 *Sci.* 41, 1-30.
- 724 Wu, F.Y., Zhao, G.C., Sun, D.Y., Wilde, S.A., Yang, J.H., 2007. The Hulan Group: its role

725 in the evolution of the Central Asian Orogenic Belt of NE China. *J. Asian Earth Sci.*  
726 30, 542-556.

727 Xiao, W.J., Windley, B.F., Hao, J., Zhai M., 2003. Accretion leading to collision and the  
728 Permian Solonker suture, Inner Mongolia, China: Termination of the Central Asian  
729 Orogenic Belt. *Tectonics* 22, 1069, doi:10.1029/2002TC001484.

730 Xiao, W.J., Windley, B.F., Huang, B.C., Han, C.M., Yuan, C., Chen, H.L., Sun, M., Sun,  
731 S., Li, J.L., 2009. End-Permian to mid-Triassic termination of the accretionary  
732 processes of the southern Altaids: Implications for the geodynamic evolution,  
733 Phanerozoic continental growth, and metallogeny of Central Asia. *International J.*  
734 *Earth Sci.* 98, 1189-1217.

735 Xu, W.L., Pei, F.P., Wang, F., Meng, E., Ji, W.Q., Yang, D.B., Wang, W., 2013a.  
736 Spatial-temporal relationships of Mesozoic volcanic rocks in NE China: constraints  
737 on tectonic overprinting and transformations between multiple tectonic regimes. *J.*  
738 *Asian Earth Sci.* 74, 167-193.

739 Xu, B., Charvet, J., Chen Y., Zhao, P., Shi, G.Z., 2013b. Middle Paleozoic convergent  
740 orogenic belts in western Inner Mongolia (China): framework, kinematics,  
741 geochronology and implications for tectonic evolution of the Central Asian Orogenic  
742 Belt. *Gondwana Res.* 23, 1342-1364.

743 Xu, B., Zhao, P., Wang, Y.Y., Liao, W., Luo, Z.W., Bao, Q.Z., Zhou, Y.H., 2015. The  
744 pre-Devonian tectonic framework of Xing'an-Mongolia orogenic belt (XMOB) in  
745 north China. *J. Asian Earth Sci.* 97, 183-196.

746 Yu, J.J., Wang, F., Xu, W.L., Gao, F.H., Pei, F.P., 2012. Early Jurassic mafic magmatism  
747 in the Lesser Xing'an-Zhangguangcai Range, NE China, and its tectonic  
748 implications: Constraints from zircon U-Pb chronology and geochemistry. *Lithos*  
749 142-143, 256-266.

750 Zhang, Q., 2014. Classification of mafic-ultramafic rocks and their tectonic significance.  
751 *Chinese Journal of Geology* 49, 982-1017 (in Chinese with English abstract).

752 Zhang, Z.C., Hao, Y.L., Wang, F.S., Mahoney, J.J., 2004. Petrology, Mineralogy and  
753 Geochemistry of the Emeishan Continental Flood Basalts, SW China: Evidence for  
754 Activity of Mantle Plumes. *Acta Geol. Sin.* 78, 40-51 .

755 Zhang, Z.C., Mao, J.W., Wang, F.S., Hao, Y.L., Mahoney, J.J., 2005. Mantle plume  
756 activity and melting conditions: Evidence from olivines in picritic-komatiitic rocks  
757 from the Emeishan Large Igneous Province, southwestern China. *Acta Geol. Sin.*  
758 28, 171-176.

759 Zhou, J.B., Cao, J.L., Wilde, S.A., Zhao, G.C., Zhang, J.J., Wang, B., 2014. Paleo-Pacific  
760 subduction-accretion: evidence from Geochemical and U-Pb zircon dating of the  
761 Nadanhada accretionary complex, NE China. *Tectonics* 33, 2444-2466.

762 Zhou, J.B., Wilde, S.A., 2013. The crustal accretion history and tectonic evolution of the  
763 NE China segment of the Central Asian Orogenic Belt. *Gondwana Res.* 23,  
764 1365-1377.

765 Zhou, J.B., Wilde, S.A., Zhang, X.Z., Zhao, G.C., Zheng, C.Q., Wang, Y.J., Zhang, X.H.,  
766 2009. The onset of Pacific margin accretion in NE China: evidence from the

767 Heilongjiang high-pressure metamorphic belt. *Tectonophysics* 478, 230-246.

768 Zonenshain, L.P., Kuzmin, M.I., Natapov, L.M., 1990. *Geology of the USSR: A Plate*

769 *Tectonic Synthesis*. American Geophysical Union, *Geodynamics Series*, 21.

770 Zorin, Y.A., 1999. Geodynamics of the western part of the Mongolia-Okhotsk collisional

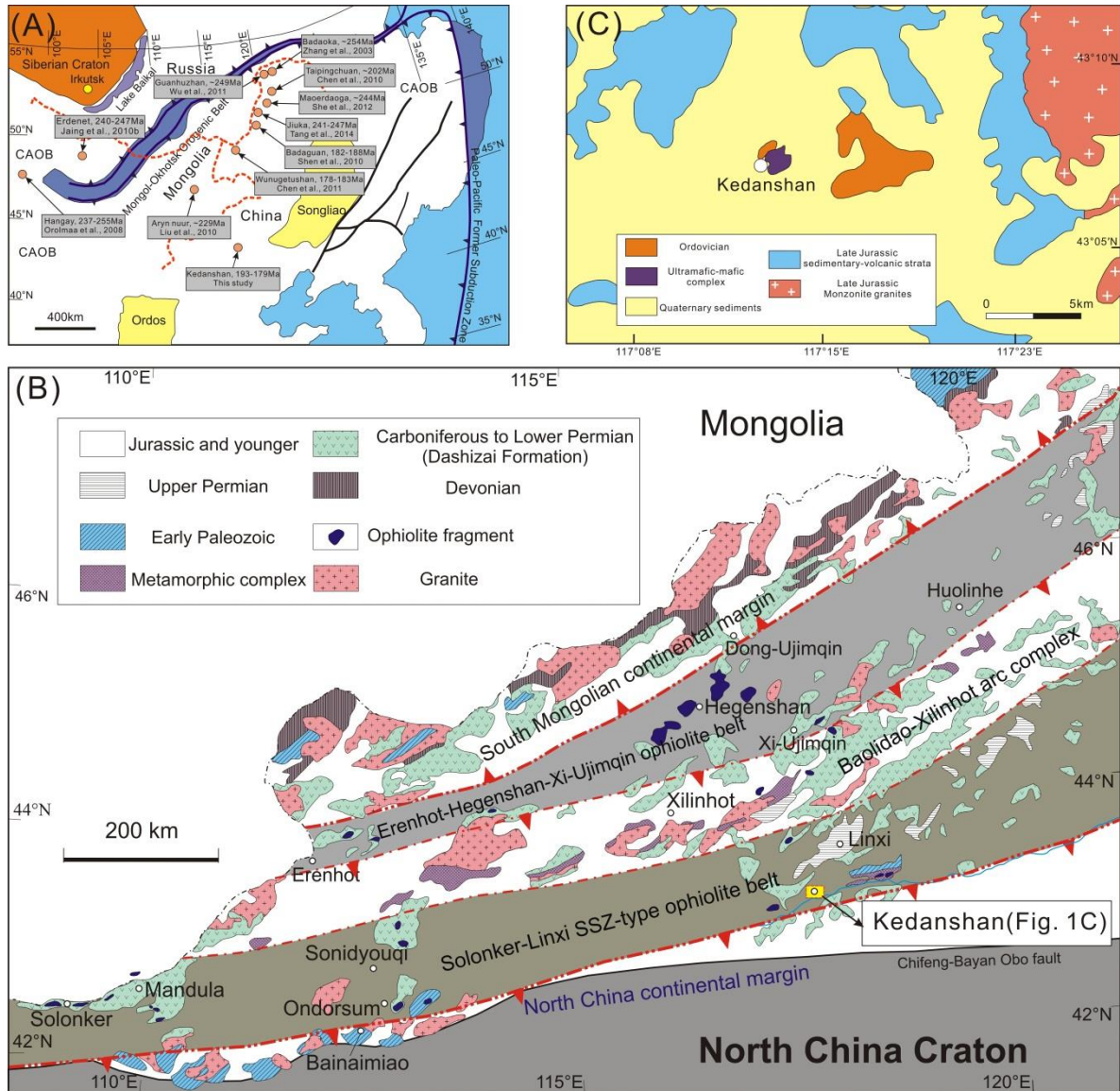
771 belt, Trans-Baikal region (Russia) and Mongolia. *Tectonophysics* 306 (1), 33-56.

772 Zhao, P., Fang, J.Q., Xu, B., Chen, Y., Faure, M., 2014. Early Paleozoic tectonic

773 evolution of the Xing-Meng Orogenic Belt: Constraints from detrital zircon

774 geochronology of western Erguna-Xing'an Block, North China. *J. Asian Earth Sci.*

775 95(38):136-146.



777

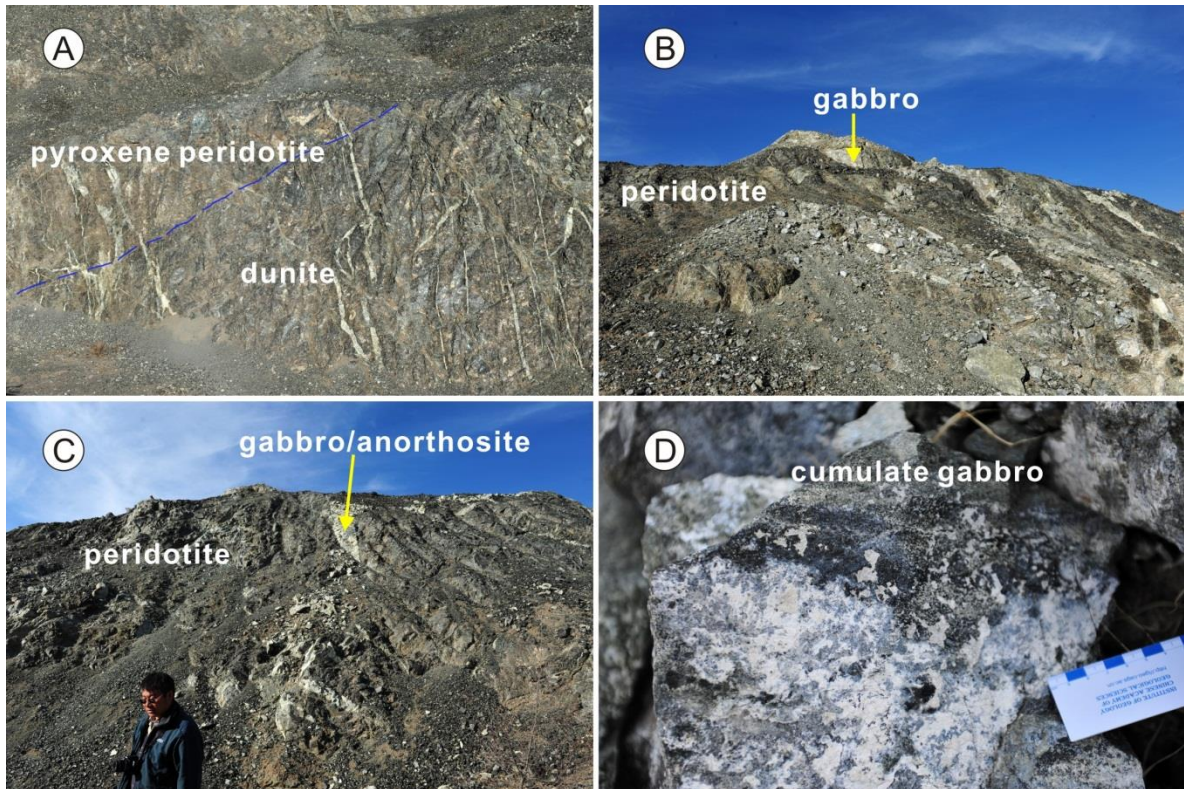
778 **Fig. 1.** (A) Sketch map showing the Mongol-Okhotsk orogenic belt, Paleo-Pacific former subduction

779 zone, and distribution of the Late Triassic to Early Jurassic igneous rocks and porphyry Cu-Mo

780 deposits, modified after Li et al. (2010) and Wang et al. (2012). (B) Geological map of the XIMAB

781 modified after Miao et al. (2007) and Song et al. (2015). (C) Simplified geological map of the

782 Kedanshan area.



783

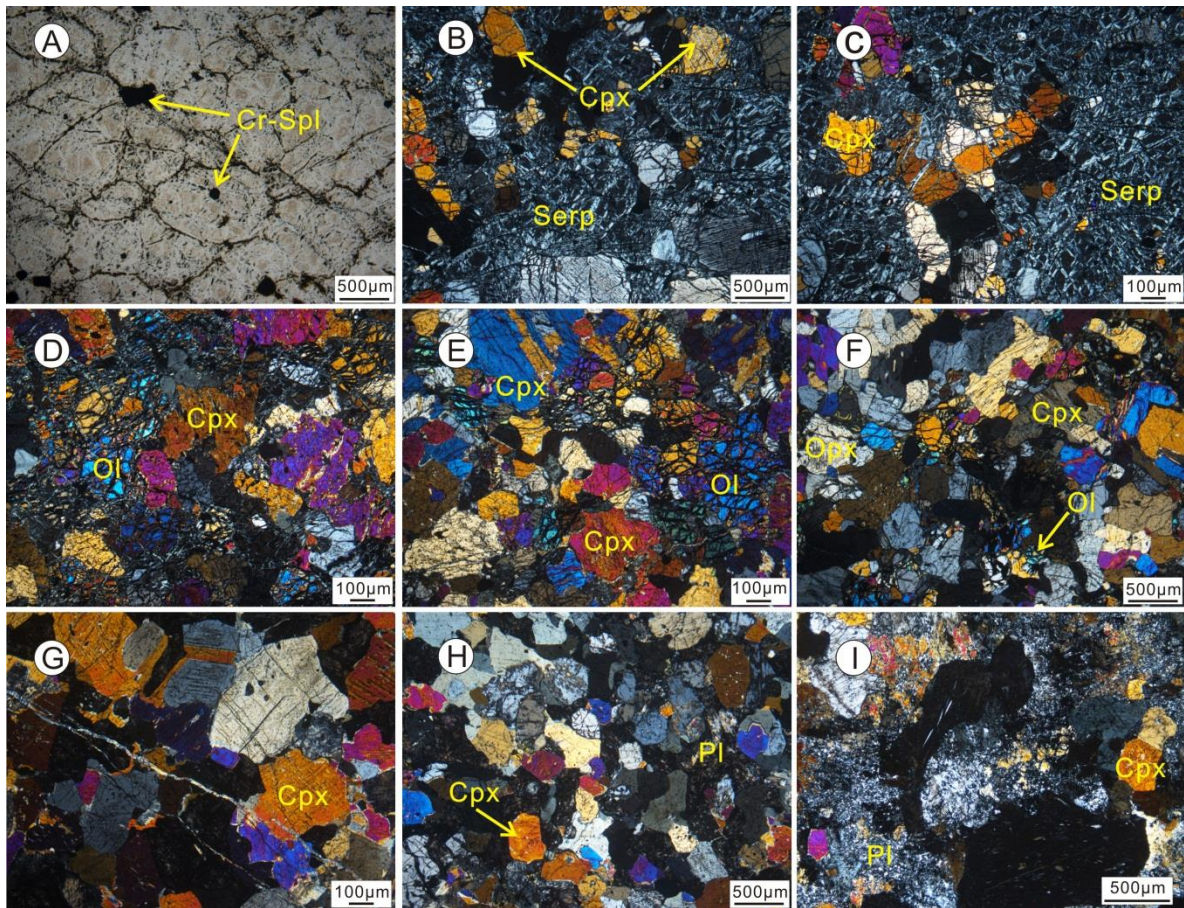
784 **Fig. 2.** Field photos from the Kedanshan ultramafic-mafic intrusion. (A) Field occurrence of dunite

785 and pyroxene peridotite, both are strongly serpentinized. The white veins are gabbro/anorthosite. (B)

786 Peridotite interlayered with gabbro. (C) Gabbro/anorthosite veins cutting the peridotite layers. (D)

787 Cumulate gabbro with layered structure.





788

789 **Fig. 3.** Photomicrographs from the Kedanshan ultramafic-mafic intrusion. (A) Strongly serpentinized

790 cumulate dunite with irregular chromian spinel without pyroxene (13LX-26). (B) Strongly

791 serpentinized dunite with ~5 vol.% clinopyroxene (13LX-14). (C) Strongly serpentinized dunite with

792 ~8 vol.% clinopyroxene (13LX-14). (D) Pyroxene peridotite with olivine > pyroxene (13LX-22). (E)

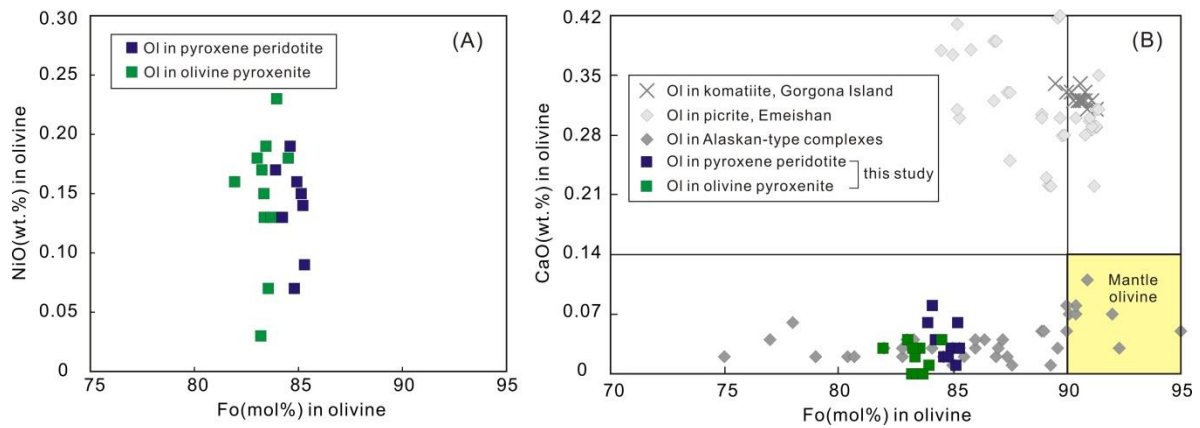
793 Pyroxene peridotite with olivine  $\approx$  pyroxene (13LX-21). (F) Olivine-bearing pyroxenite with olivine

794  $\ll$  pyroxene (13LX-20). (G) Plagioclase-poor pyroxenite with plagioclase  $\ll$  pyroxene (13LX-18). (H)

795 Cumulate gabbro with plagioclase < pyroxene (13LX-27). (I) Plagioclase-rich cumulate gabbro with

796 plagioclase  $\gg$  pyroxene (13LX-19).

797



798

799 **Fig. 4.** (A) NiO versus Fo number diagram and (B) plot of CaO versus Fo number (modified after Li

800 et al., 2012b) for olivines from the Kedanshan ultramafic-mafic intrusion. Komatiite data from

801 Kamenetsky et al. (2010); picrite data from Zhang et al. (2004, 2005); Alaskan-type complexes data

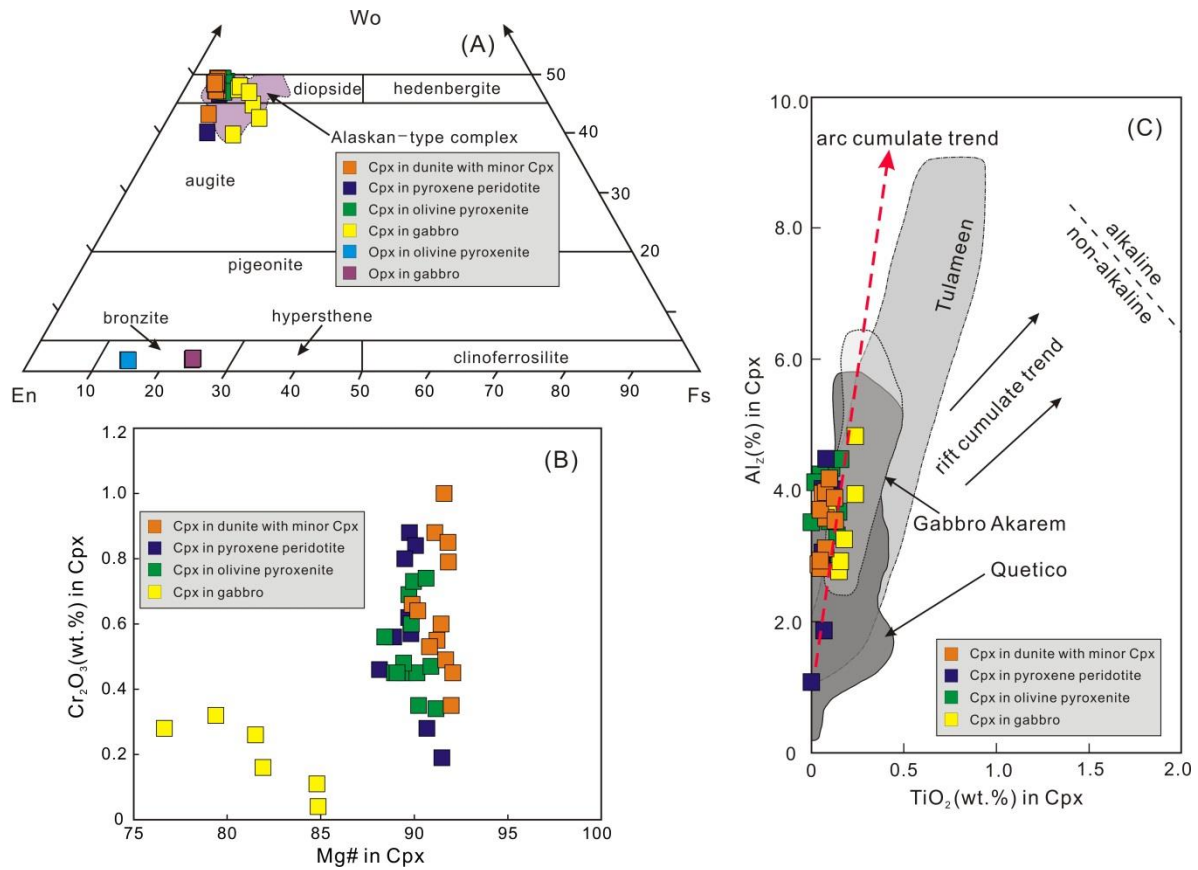
802 from Li et al. (2012b) and Krause et al. (2007).

803

804

805

806



807

808 **Fig. 5.** (A) Wo-En-Fs diagram (Morimoto, 1988) for pyroxenes from the Kedanshan ultramafic-mafic

809 intrusion. (B) Variation diagram of Mg# versus  $Cr_2O_3$  wt.% for clinopyroxenes from the Kedanshan

810 ultramafic-mafic intrusion. (C)  $Al_z$  (percentage of tetrahedral sites occupied by Al) versus  $TiO_2$  (wt.%)

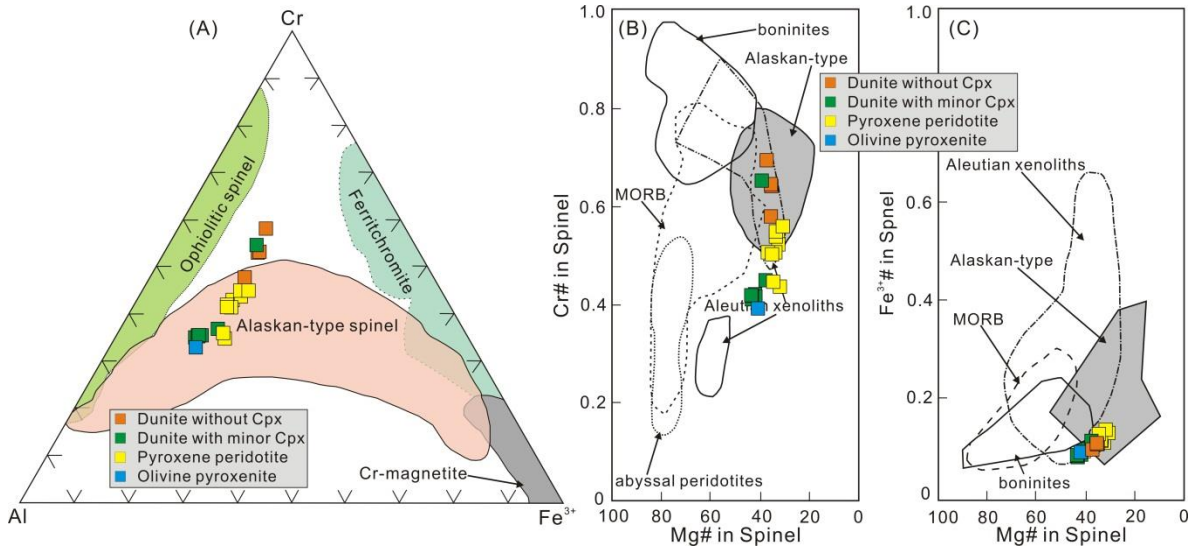
811 plot for clinopyroxenes from the Kedanshan ultramafic-mafic intrusion. The gray fields are typical

812 Alaskan-type complexes worldwide. Quetico data are from Pettigrew and Hattori (2006), Tulameen

813 from Rublee (1994), Gabbro Akarem from Helmy and EI Mahallawi (2003). Alkaline and

814 non-alkaline field, arc cumulate trend and rift cumulate trend are from Le Bas (1962) and Loucks

815 (1990).



816

817 **Fig. 6.** (A) Cr-Al-Fe<sup>3+</sup> triangle plot of chromian spinels from the Kedanshan ultramafic-mafic

818 intrusion. Discriminating fields from Irvine (1967), Barnes and Röeder (2001), Helmy and El

819 Mahallawi (2003) and Farahat and Helmy (2006). (B) Plot of Cr# versus Mg# of chromian spinels

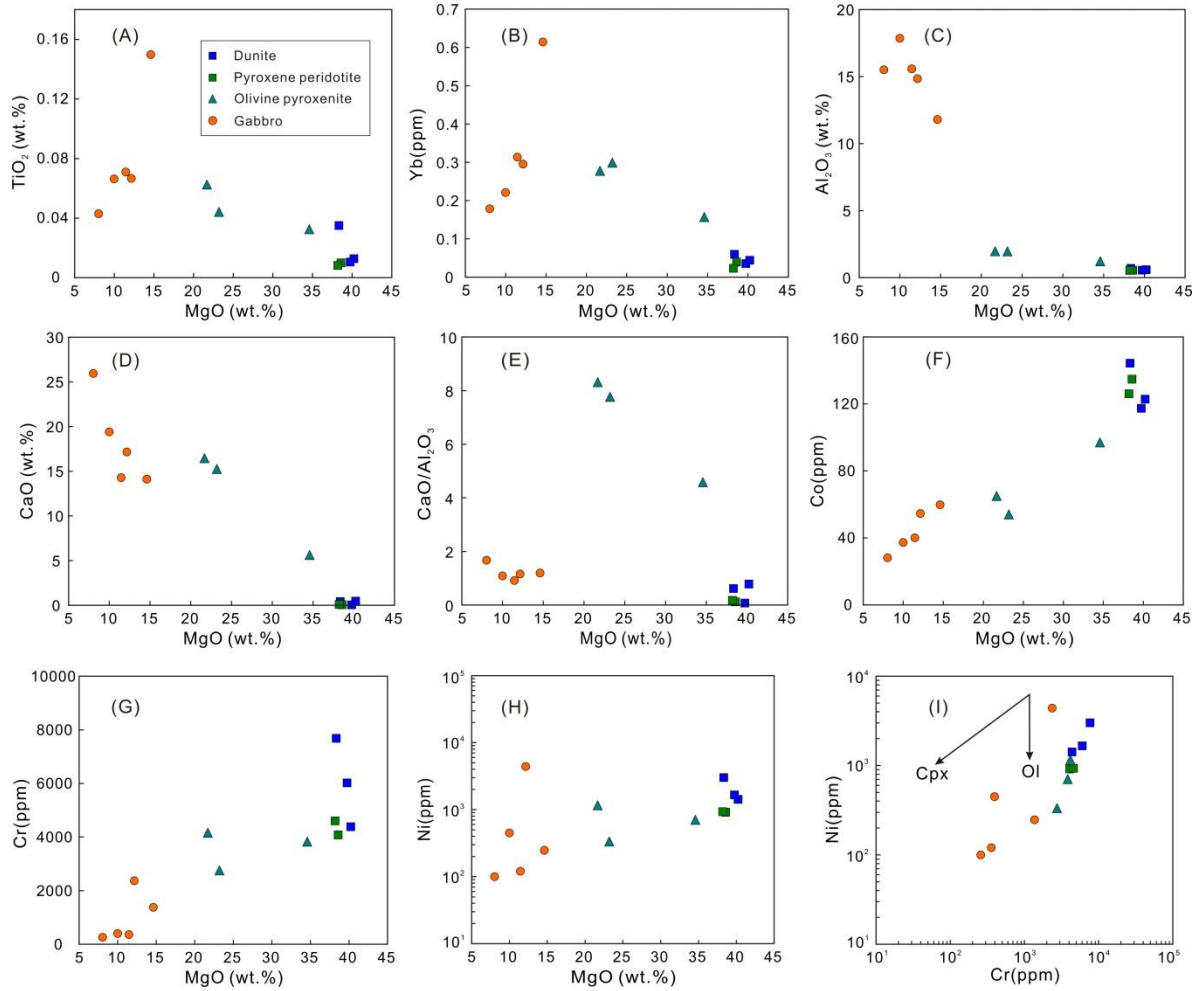
820 from the Kedanshan ultramafic-mafic intrusion. (C) Plot of Fe<sup>3+</sup># versus Mg# of chromian spinels

821 from the Kedanshan ultramafic-mafic intrusion. MORB and boninite fields from Barnes and Roeder

822 (2001), abyssal peridotite field from Dick and Bullen (1984), Alaskan-type field from Burns (1985)

823 and Himmelberg and Loney (1995), Aleutian pyroxenite and gabbro xenoliths fields from Conrad and

824 Kay (1984), DeBari et al. (1987), DeBari and Coleman (1989).



825

826 **Fig. 7.** Plots of MgO versus oxides and compatible elements from the Kedanshan ultramafic-mafic

827 intrusion.

828

829

830

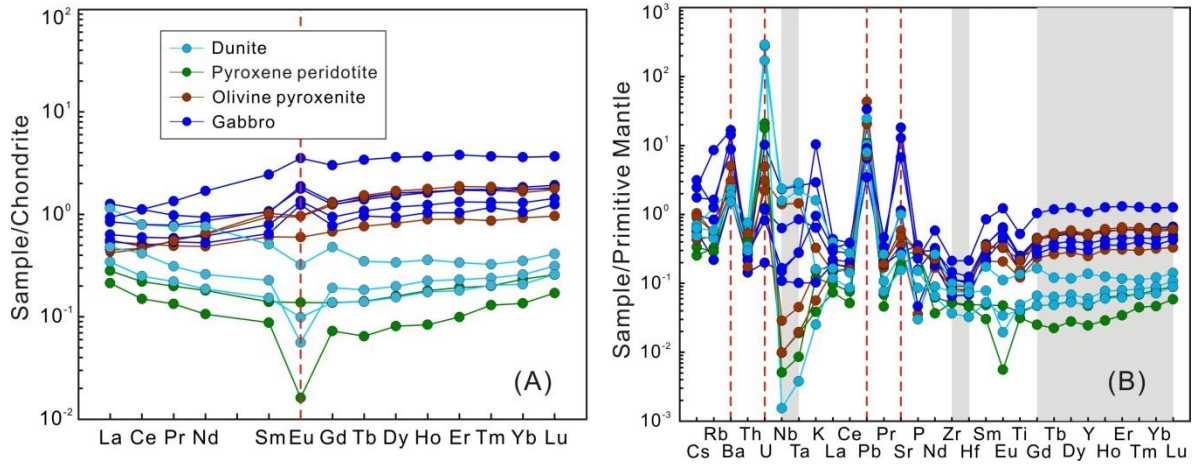
831

832

833

834

835

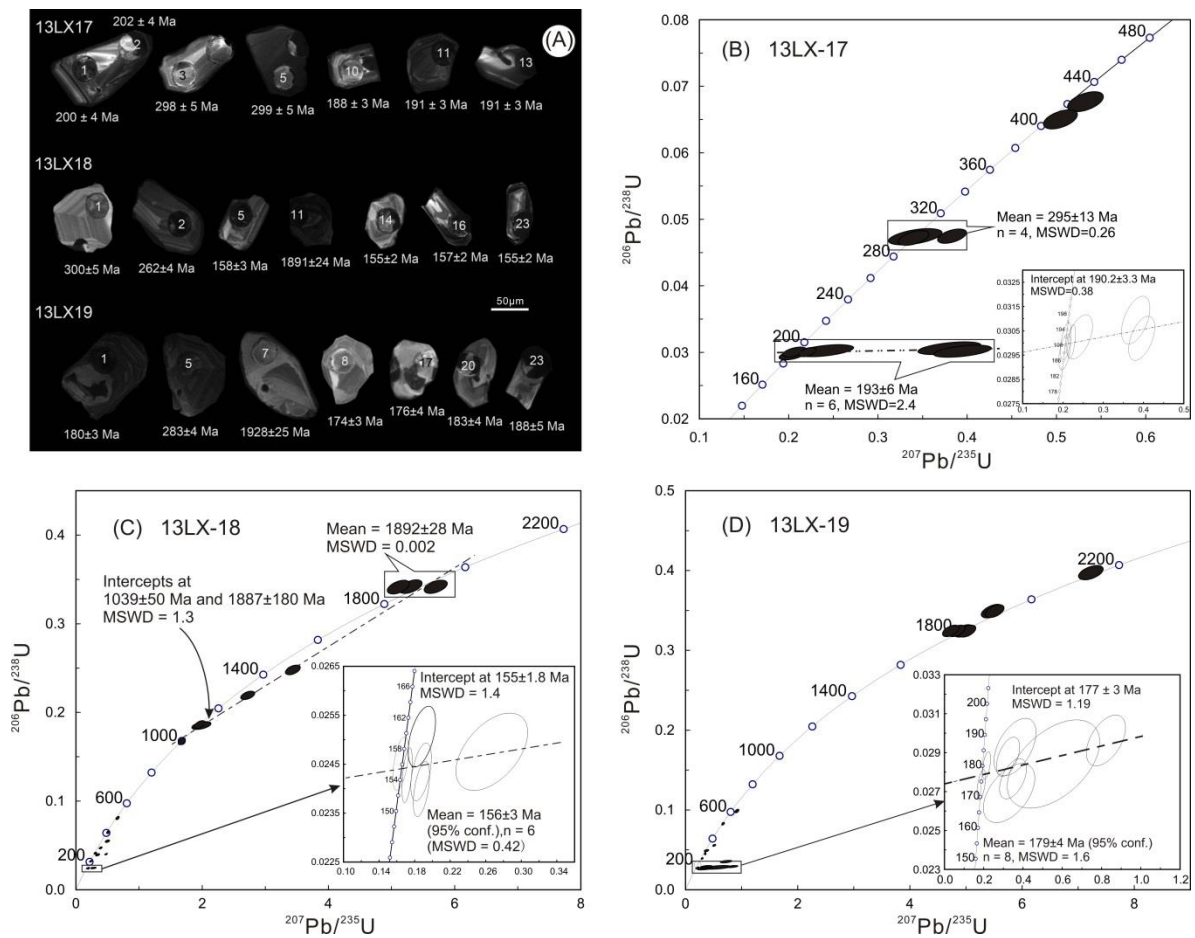


836

837 **Fig. 8.** Chondrite-normalized REE and primitive mantle-normalized multi-element patterns from the

838 Kedanshan ultramafic-mafic intrusion. Chondrite and primitive mantle normalizing values after Sun

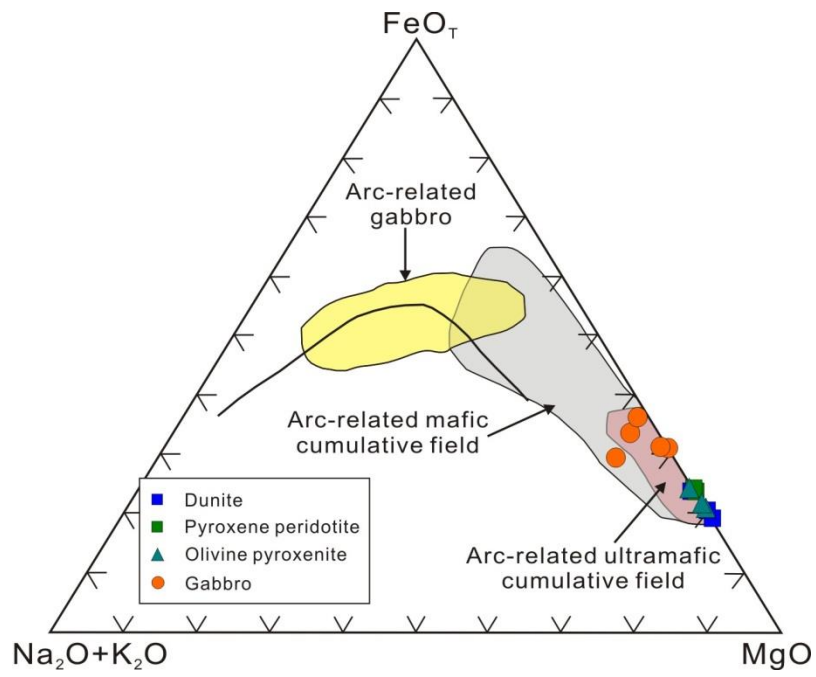
839 and McDonough (1989).



840

841 **Fig. 9.** CL images and concordia diagrams of zircon LA-ICP-MS analyses of gabbro samples from the

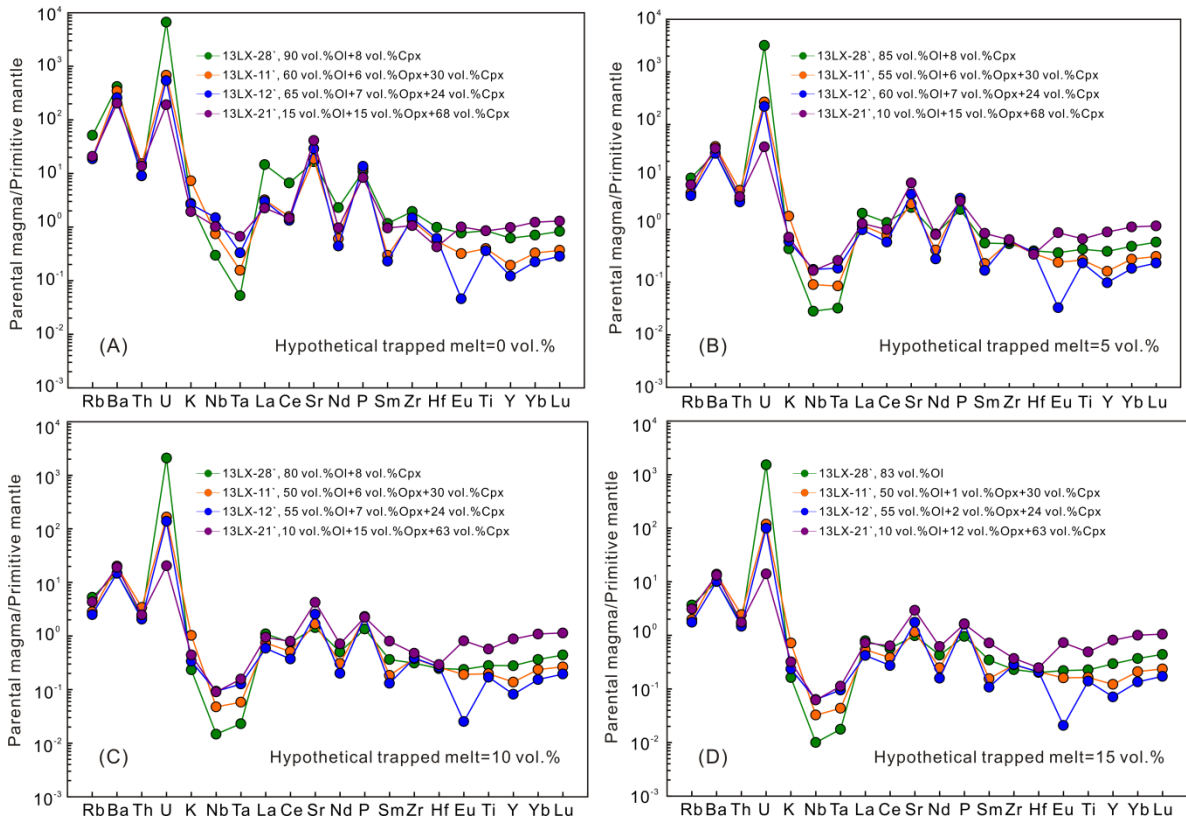
842 Kedanshan ultramafic-mafic intrusion.



843

844 **Fig.10.** AFM diagram from the Kedanshan ultramafic-mafic intrusion (modified after [Beard, 1986](#)).

845



846

847 **Fig.11** Primitive mantle-normalized multi-element patterns from the calculated parental magma

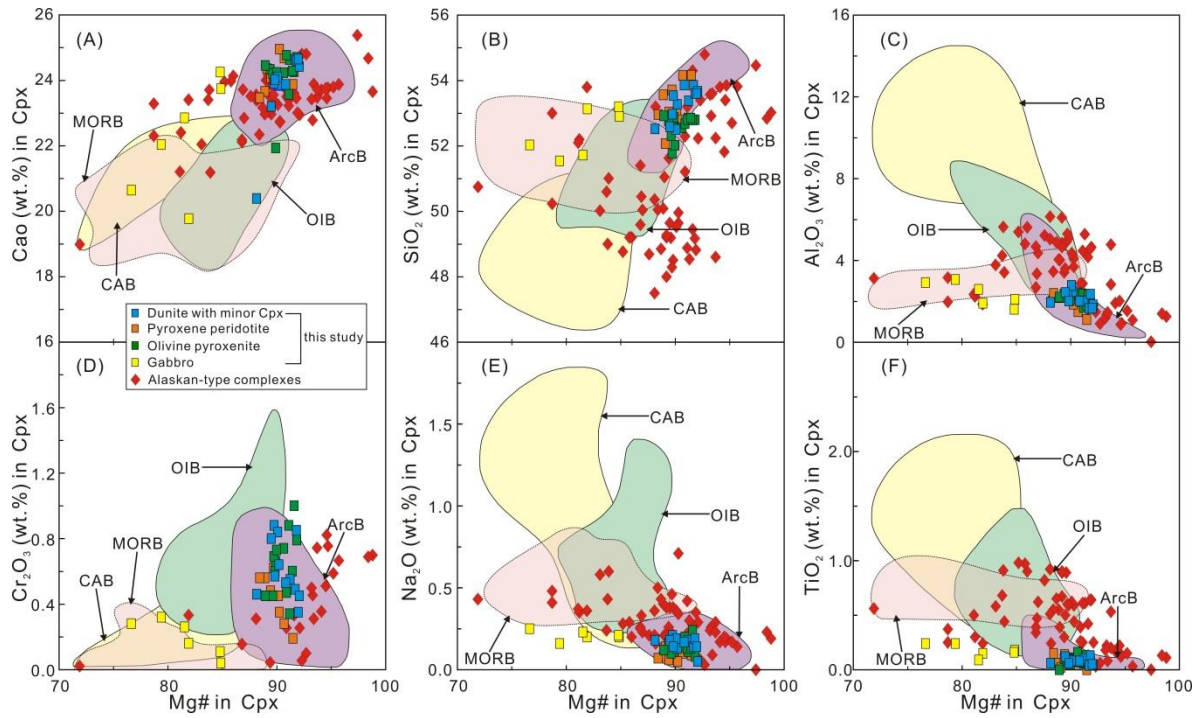
848 compositions of the Kedanshan ultramafic-mafic intrusion. Normalization values of PM are from [Sun](#)

849 [and McDonough \(1989\)](#).

850

851





852

853 **Fig. 12.** Mg# versus major element contents in clinopyroxenes from the Kedanshan ultramafic-mafic

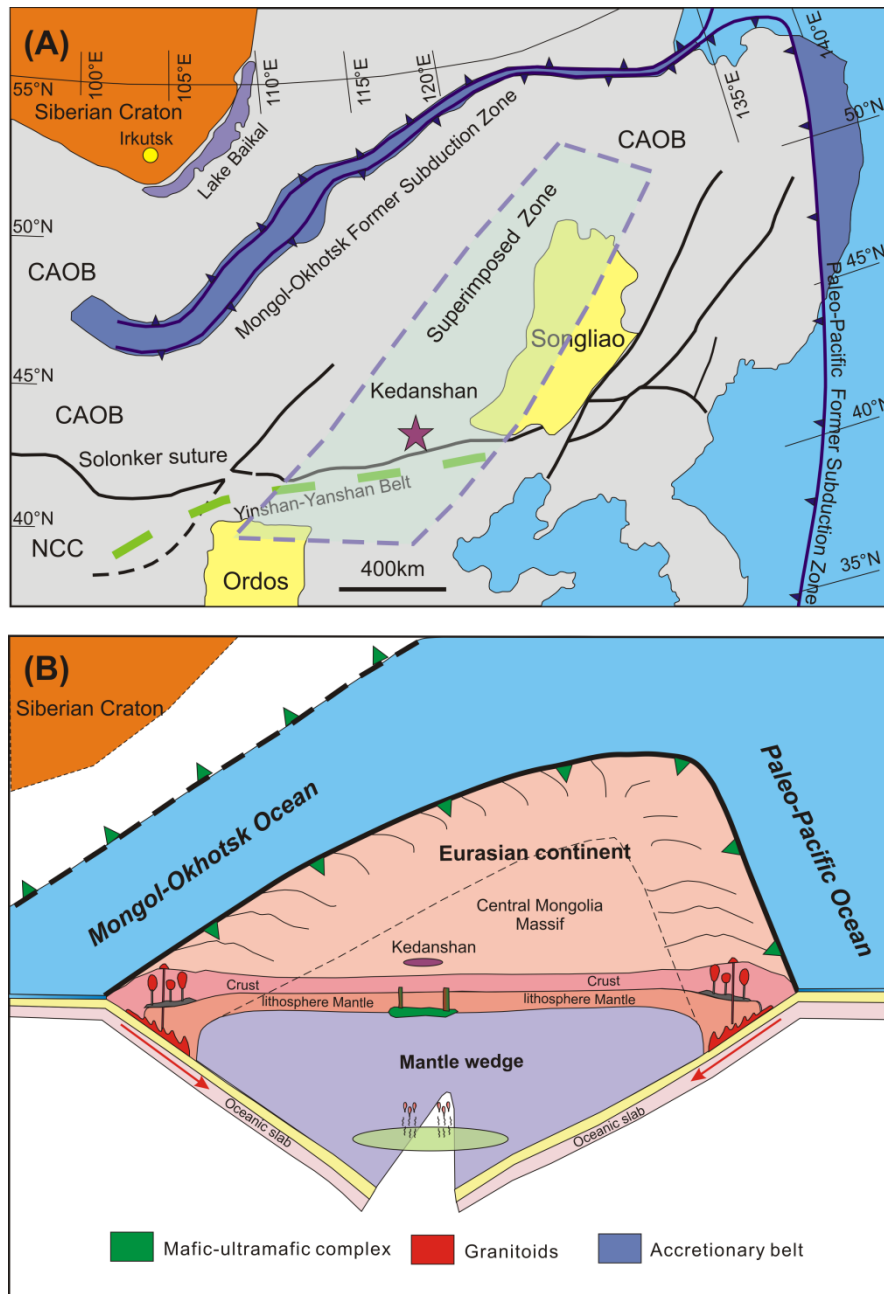
854 intrusion. Cpx composition fields from magmatic cumulate dunite, wehrlite, and clinopyroxenite

855 xenoliths hosted in arc basalts (ArcB), oceanic island basalts (OIB) and continental alkaline basalts

856 (CAB) after [Kim and Choi \(2016\)](#) and references therein; Cpx composition field from gabbros and

857 gabbroic rocks in MORB after [Niu et al. \(2002\)](#); Cpx compositions from Alaskan-type complexes

858 after [Himmelberg and Loney \(1995\)](#).



859

860 **Fig. 13.** A tectonic model showing a petrogenetic link between the Jurassic Kedanshan  
 861 ultramafic-mafic intrusion and superimposed subduction. (A) A sketch map showing location of the  
 862 Kedanshan ultramafic-mafic intrusion and former subduction zones of the Mongol-Okhotsk Ocean  
 863 and Paleo-Pacific Ocean (modified after Wang et al., 2012). (B) A cartoon showing superimposed  
 864 subduction of the Mongol-Okhotsk Ocean and Paleo-Pacific Ocean beneath the Central Mongolia  
 865 Massif.